Article

Movement is governed by rotational neural dynamics in spinal motor networks

https://doi.org/10.1038/s41586-022-05293-w

Received: 28 September 2021

Accepted: 30 August 2022

Published online: 12 October 2022

Check for updates

Henrik Lindén[1]✉, Peter C. Petersen[1], Mikkel Vestergaard[1,2] & Rune W. Berg[1]✉

Although the generation of movements is a fundamental function of the nervous system, the underlying neural principles remain unclear. As flexor and extensor muscle activities alternate during rhythmic movements such as walking, it is often assumed that the responsible neural circuitry is similarly exhibiting alternating activity[1]. Here we present ensemble recordings of neurons in the lumbar spinal cord that indicate that, rather than alternating, the population is performing a low-dimensional 'rotation' in neural space, in which the neural activity is cycling through all phases continuously during the rhythmic behaviour. The radius of rotation correlates with the intended muscle force, and a perturbation of the low-dimensional trajectory can modify the motor behaviour. As existing models of spinal motor control do not offer an adequate explanation of rotation[1,2], we propose a theory of neural generation of movements from which this and other unresolved issues, such as speed regulation, force control and multifunctionalism, are readily explained.

The neural circuitry behind movement encompasses several distinct forebrain regions, the cerebellum and the brainstem. The core executive circuits for movement such as locomotion, however, reside in the spinal cord[3]. These spinal motor circuits, often referred to as central pattern generators (CPGs), are capable of autonomous generation of rhythmic coordination of muscles. Although great progress has been made in characterizing the cellular properties of spinal interneurons and motor neurons, including their genetic lineages[4,5], the detailed network architecture and the associated neuronal ensemble dynamics remain elusive. Owing to the apparent right–left and flexor–extensor alternation, it has often been proposed that distinct groups of interneurons, or 'modules', are active in a push–pull fashion and that the rhythm is ensured by cellular pacemaker properties[1,2]. It is unknown whether and how such organization and different motor programs are manifested in ensemble activity of spinal networks.

Rotation in spinal motor circuits

Here we examined the activity in spinal motor networks using extracellular multi-electrode recording in the turtle lumbar spinal cord. This preparation provided mechanical stability, which allowed simultaneous monitoring of large numbers of spinal interneurons in laminae VII–VIII and motor neurons during the execution of various rhythmic motor programs[6–8]. The firing rate of individual neurons was close to sinusoidal (Extended Data Fig. 1) and, as expected, rhythmic in relation to the nerves, but the population activity as a whole seemed incomprehensible (Fig. 1a,b). However, when sorting these neurons according to the phase of the motor nerve output, we found that the population activity resembled a continuous sequence, which covered all phases of the cycle (Fig. 1c). To better understand the sequential activity, we performed a principal component analysis of both the neuronal population and the nerve activity. Both the neuronal activity and the six motor nerves followed a low-dimensional manifold (that is, most variance was explained by few components; Fig. 1d). Whereas the nerve activity seemed entangled, the neuronal activity had a simple rotation (Fig. 1e,f). Rotational population activity was independent of the sorting, and it was observed in all trials and across animals (Extended Data Figs. 1 and 2 and Supplementary Video 1). To quantify this distinction further, we applied a previously defined metric[9], which quantifies the 'tangling' of neural trajectories (that is, the degree to which points along the trajectory are close to each other, but move in different directions). We found the tangling to be larger for the muscle trajectories than the neuronal trajectories most of the time (>96.3%), which was consistent across datasets (Extended Data Fig. 3). As the tangling for rotational trajectories is lower than for trajectories with points that are close to each other and moving in the opposite direction, as would be the case for alternating activity (Extended Data Fig. 3a), these data are consistent with a neuronal population that is executing a rotation. There did not seem to be any discrete phase preference as otherwise expected in an alternating modular network (Extended Data Figs. 1–3). Rotational dynamics has been observed in the motor cortex and elsewhere[10–12], but it has not been described for spinal circuits previously. Nevertheless, indications can be found as wide phase distributions in the scarce literature on spinal population recordings[6,13–15].

Theory to explain rotation

As conventional CPG theories, which are founded on a push–pull organization with intrinsically rhythmic modules[16,17], do not readily explain rotational dynamics, we sought to explore a theory that can account for this and other open questions in spinal motor control. In particular, the mechanisms for generation of rhythms have remained nebulous. Cellular pacemaker properties have been suggested[1], but decades of research have not been able to pinpoint a responsible cell type[17].

[1]Department of Neuroscience, Faculty of Health and Medical Sciences, University of Copenhagen, Copenhagen, Denmark. [2]Present address: Department of Neuroscience, Max Delbrück Center for Molecular Medicine, Berlin, Germany. ✉e-mail: hlinden@sund.ku.dk; runeb@sund.ku.dk

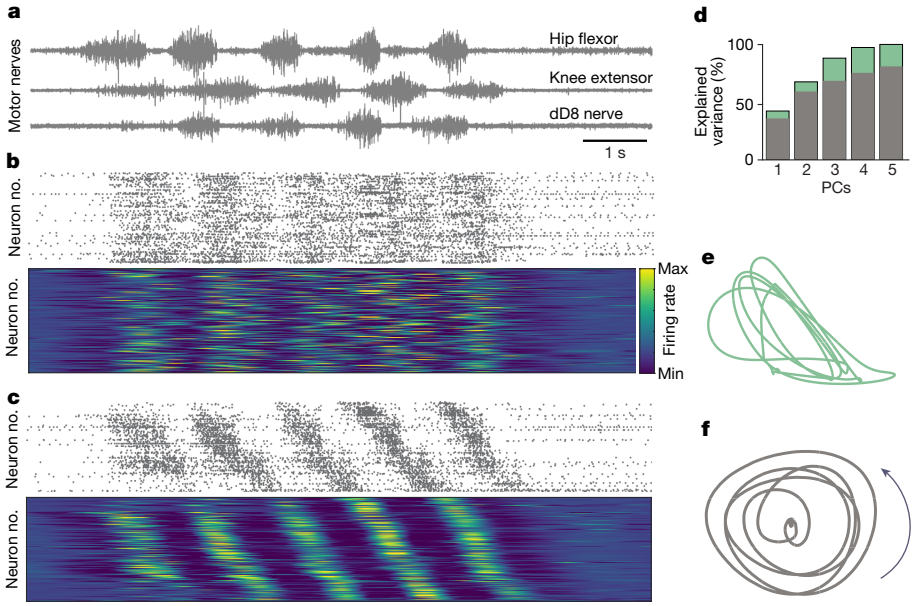

Fig. 1 | Neuronal population activity in the lumbar spinal cord has rotational dynamics. a, The activities of three selected motor nerves (electroneurogram) during rhythmic hindlimb scratching movement. **b**, Concurrent ensemble activity of spinal neurons in the turtle lumbar spinal cord as a raster plot (top, $n = 214$) and estimated firing rates (bottom). **c**, Sorting the neurons in **b** according to phase (hip flexor) reveals sequential activity. **d**, The first PCs explain most variance of electroneurogram activity (green) and neuronal ensemble activity (grey). **e**,**f**, The first two PCs of nerve activity (**e**) and neuronal population (**f**). Tangling of the nerve activity was higher than that of the network 96% of the time. One out of ten samples shown. Similar experiments repeated in five independent data sessions (four animals) with a total of 28 trials of one behaviour.

Here we propose that the rhythm arises as a network oscillation rather than through cellular properties. It is well known that a network that is close to the transition point of dynamical instability can have rhythmogenic properties without requiring specific cellular properties[18]. As the CPG network structure is unknown, we assumed a structure in which glutamatergic neurons were randomly and recurrently connected. To prevent catastrophic runaway activity[19,20], the excitation (E) was balanced by recurrent glycinergic inhibition (I) (Fig. 2a,b), in line withreports of balanced synaptic input in various motor circuits[21–23]. Balanced networks of this type are known to undergo a phase transition when synaptic weights are increased beyond a critical value[24,25]. For large networks, activity in this regime is chaotic[26], whereas finite-sized networks in a dynamical regime close to the transition point may exhibit more regular activity[27]. A linearization of the dynamics

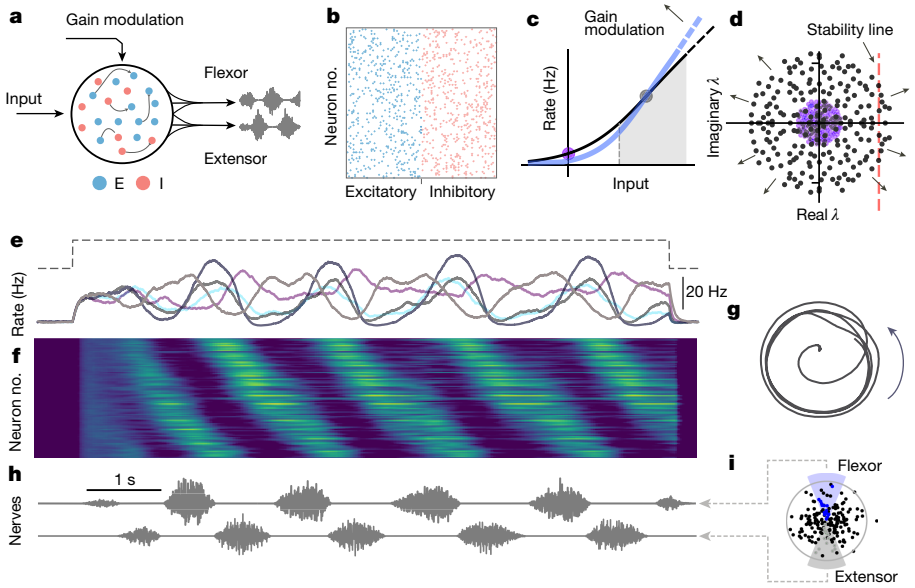

Fig. 2 | Rotational dynamics emerges in the BSG model. a, The BSG model. An input drive activates a recurrent network with excitatory (blue) and inhibitory (red) neurons. The network can receive both synaptic input and gain modulation. A subset of cells provides motor output. **b**, The connectivity matrix has 50% excitation and inhibition. **c**,**d**, The firing rate is increased by synaptic input (bottom arrow; **c**), causing the eigenvalue spectrum to expand (purple versus grey, **d**) and cross the stability line (dashed red line, **d**) and thus generate a network oscillation. A gain modulation results in a change in slope (blue line and arrow, **c**). **e**, Input (top) and firing rates of five neurons (bottom). **f**, Sequential activity revealed by sorting according to phase, similar to experiments. **g**, Projection of the population firing rates on the two first PCs reveals a rotation. **h**, The model nerve output displays alternating activity. **i**, Flexor and extensor nerves are innervated by antiphase excitatory neurons in the strongest eigenmode (blue and grey, respectively).

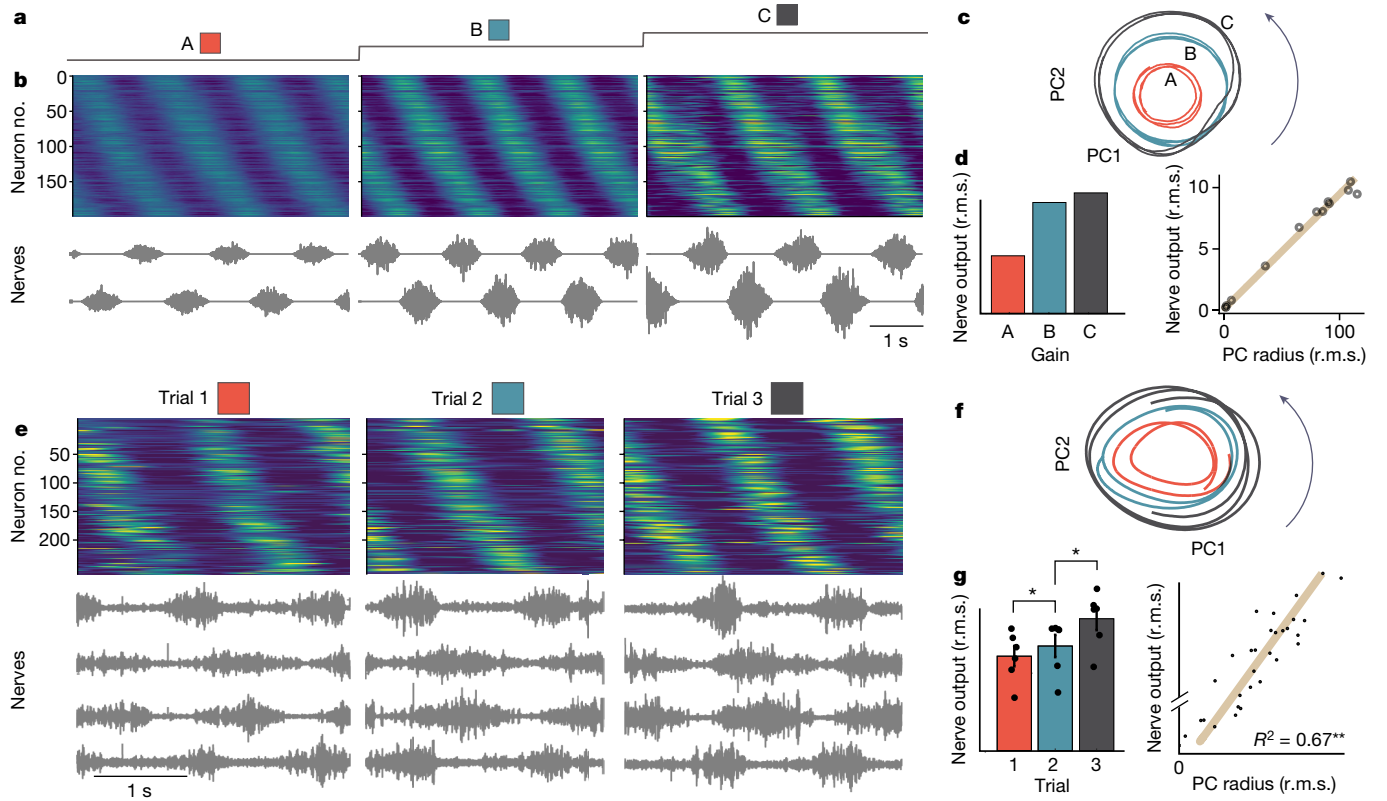

Fig. 3 | Network control of amplitude in the BSG model. a,**b**, Increasing the common gain in the network (A–C; **a**) ramps up ensemble activity (**b**, top) and nerve output (**b**, bottom). **c**, Higher firing rates are associated with a larger radius of rotation in PC space (colour-matched with levels A–C). **d**, Correlation of radius (right) and gain (left) with nerve output. **e**,**f**, Experimental verification through trials 1–3 with different nerve outputs and radii (**f**, colour-matched). **g**, Nerve amplitude (r.m.s. ± s.e. of six nerves) versus radius of rotation (r.m.s. of PC1 and PC2); one-sided Wilcoxon test (*P = 0.016); linear regression, **P < 0.01, F-statistics, null hypothesis of zero correlation.

close to this point (see the mathematical note in the Supplementary Information) demonstrates that finitely sized networks can generate oscillatory activity if the leading eigenvalue of the connectivity matrix has a nonzero imaginary part[27]. On the basis of this idea, we set up a model network of rate-based neurons with sparse connectivity for which an external input, in the form of a synaptic drive (for example, sensory related or descending from the brain), could move the eigenvalues of the connectivity matrix across the stability line owing to a change in the set point of the firing-rate function (Fig. 2c,d). A second type of input that modulates the gain of individual neurons[28] was also included to provide a mechanism to modify the network state. As the network received a sustained synaptic input, some of the eigenvalues moved beyond a critical level (red dashed line), which caused firing rates in the network to exhibit self-sustained rhythmic activity (Fig. 2d,e). When sorting the neurons according to phase, a sequential activity was revealed (that is, a rotation), similar to the experimental observations (Fig. 2f,g). We refer to a network in this state as a balanced sequence generator (BSG). Both the BSG model and the experimentally observed rotation are fundamentally different from conventional models, which are founded on alternation with the neurons having clustered phase preferences and belonging to modules composed exclusively of either excitatory or inhibitory neurons.

To model the output nerve activity from the BSG model, we connected a subset of neurons on the basis of their phase in the dominant eigenmode to pools of motor neurons to provide the appropriate nerve activity. This resulted in an alternating nerve output resembling the experimental observations (Fig. 2h,i and Supplementary Video 2). Next we investigated the activity of the excitatory and inhibitory populations during the motor program in the BSG model. We found that both the E and I populations themselves exhibit similar sequences as the combined population activity (Extended Data Fig. 4). These results demonstrate that rotational dynamics can arise in simple networks without fine-tuning of parameters and result in an alternating nerve output, in line with our experimental findings (Supplementary Video 2). Although proprioceptive feedback from muscles and their reflexive circuitry was not included in the BSG model, we expect this feedback to improve the performance by stabilizing the rhythmic activity.

Control of force and period

Next we evaluated whether the BSG model could explain previously unsolved issues, such as independent control of force and speed of the movement. The ability to modulate the strength of the output and speed is key for volitional control but, to our knowledge, no mechanism has been proposed for controlling these independently. To investigate these aspects in the model, we used gain modulation (that is, the slope; Fig. 2c) of the neuronal firing-rate function around the working point set by the external input[28]. First, we found that collective (uniform) modulation of the gain by an input drive could indeed control the amplitude in the BSG model (Fig. 3a–c). As the amplitude increased, so did the radius of rotation, whereas the frequency and sequence remained largely unaltered (Extended Data Fig. 5). To verify this prediction experimentally, we inspected trials that, owing to an inherent variability, had various radii of rotation (Fig. 3e and Extended Data Fig. 1f). The radius of rotation had substantial correlation with the motor nerve activity (Fig. 3f,g and Extended Data Fig. 6), in line with the predictions from the BSG model and the proposed mechanism for amplitude control.

Next we explored whether the BSG model could control the period of the rhythm and thereby the speed of movement execution. Rather than collectively adjusting the neuronal gain of all neurons in the network,

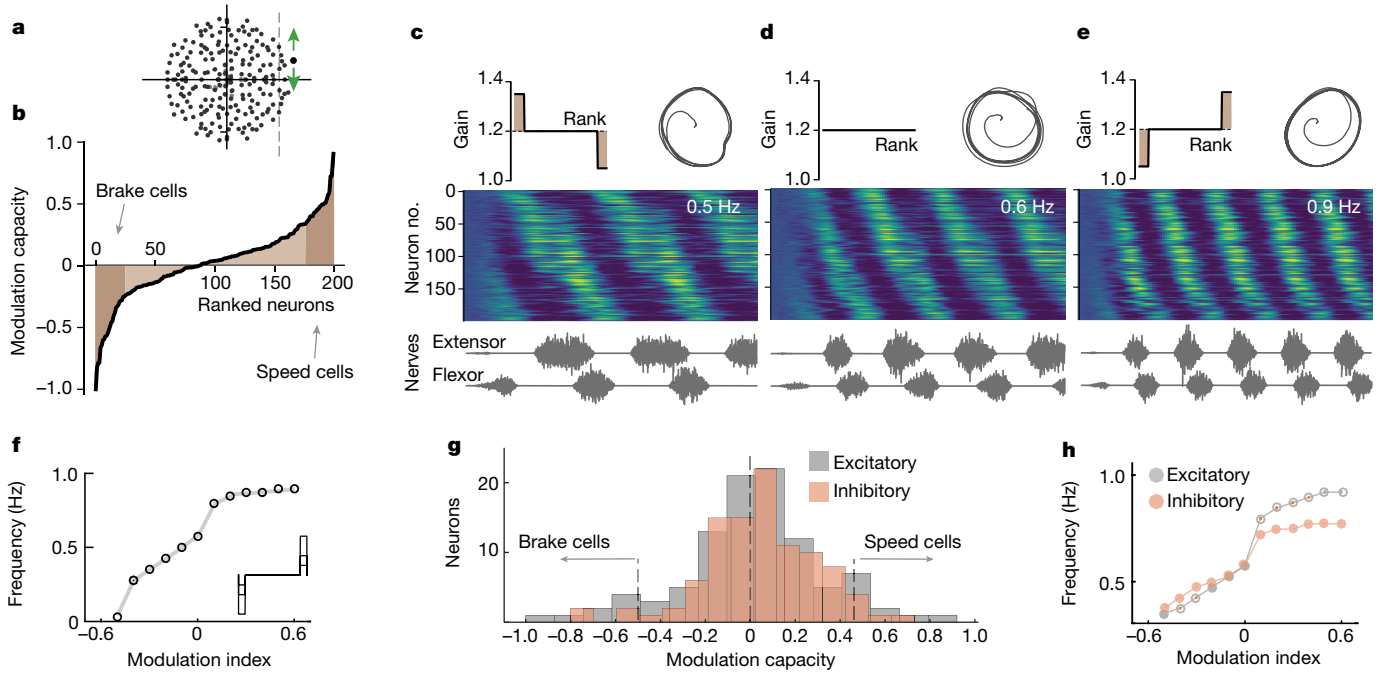

Fig. 4 | Modulation of period in the BSG model. a, Adjusting the neuronal gain to change the rhythm by moving the eigenvalue up or down (green arrows). **b**, Capacity to modulate the rhythm by an individual neuron is assessed by changing its gain. Ranking neurons accordingly reveals brake and speed cells. **c**,**d**, When activating brake cells while impeding speed cells (gain profile, top left), the rhythm is slowed down (**c**) compared with neutral (**d**). Middle, sorted ensemble activity; bottom, nerve output. The radius of rotation is largely unchanged (PCs top right), indicating a similar amplitude of motor output. **e**, Reversed activation results in a faster rhythm (0.9 Hz). **f**, Gradually modulating the speed and brake cells (inset) can either decrease or increase the frequency. **g**, The capacity to modulate the rhythm has a bell-shaped distribution. Brake and speed cells represent cells with strong modulation capacity, in which both excitatory and inhibitory cells are found. $n = 200$. **h**, Modulating only excitatory (grey) or inhibitory (orange) cells is sufficient to change the frequency.

we found that selective gain modulation of a subset of neurons could alter the frequency of the population activity without affecting the amplitude (Fig. 4). Individual gain modulation is a powerful tool in network control[28], and here we systematically tuned the neuronal gain to identify a subset of neurons that had most influence on the period (Fig. 4a–f). Some neurons had a strong positive or negative effect, which we call brake and speed cells, respectively, whereas others had minor effects on the rhythm. There were both inhibitory and excitatory neurons among both the speed and brake cells (Fig. 4g,h). Interestingly, cells with a speed-modulating capacity have been demonstrated experimentally[29,30]. However, as both excitatory and inhibitory neurons were found among the brake and speed cell categories in our model, an experimentally testable predication would be that also inhibitory neurons can have similar speed-modulating effects. The modulation capacity of individual neurons in the model is not due to their cellular properties, but rather their specific location in the network structure. A possible link between the network location, cell identity and speed control remains to be assessed.

Multiple motor programs

The ability to execute multiple motor behaviours (that is, a multifunctional output) is the hallmark of the motor system[31,32]. Although cortical network models have already been demonstrated to generate multifunctional output[33,34], contriving a model within the conventional framework of spinal motor circuits that can accommodate the rich repertoire of behaviours has so far been a major challenge. Here we focused on two well-known motor behaviours in the turtle and investigated these both experimentally and in the model. These behaviours consist of hindlimb movements, in which either the knee is protracted while moving the foot in small circles (pocket scratching) or the foot is protracted while the leg is stretched (rostral scratching)[35]. We reasoned that this multifunctional activity is caused by a perturbation of the rotational dynamics that in turn switches the phases of the resulting motor nerve outputs. To test this idea in the BSG model, we identified two subsets of neurons for which two distinct sets of gain modulation (gain profiles, Fig. 5a,b and Supplementary Video 3) caused a moderate change in the phase preference of individual neurons. A comparison of the resulting neuronal phase preferences between the two behaviours indicated that many of the neurons kept their timing in the sequence (Fig. 5f,g). We then optimized a set of readout weights to drive motor nerve activity that caused a phase shift of the hip angle between the two behaviours (Fig. 5c). In the resulting simulation, the nerve output of behaviour 1 had knee and hip extensors in phase ('no shift', Fig. 5d), whereas the second input pattern caused the phase of the hip extensor (and flexor) to change in relation to that of the knee extensor (Fig. 5e). Despite the marginal visual differences in population activity between the two behaviours (compare Fig. 5d,e and Supplementary Video 3), the network generated markedly different motor outputs. Using principal component analysis, we found that the switch between behaviours was associated with a change of the low-dimensional subspace of the rotational dynamics. When projecting the population activity of behaviour 2 onto the principal components (PCs) for behaviour 1 (red), the rotational dynamics had a smaller variance compared to the variance of behaviour 1 (black; Fig. 5h). However, a comparison with the variance of the projection of the 'native' PCs of behaviour 2 (not shown) showed that this was not due to a markedly lower variance of behaviour 2 compared to behaviour 1, but instead that a fraction of the variance was in another subspace. By computing the ratio between the variance explained in these two subspaces[36], we quantified the subspace overlap between the two behaviours to be 0.49. These model results were qualitatively similar to the experimental data, in which the sequential activation, although not identical, remained during the two behaviours (Fig. 5i–m). The subspace overlap here was 0.34 (Fig. 5m). A similar

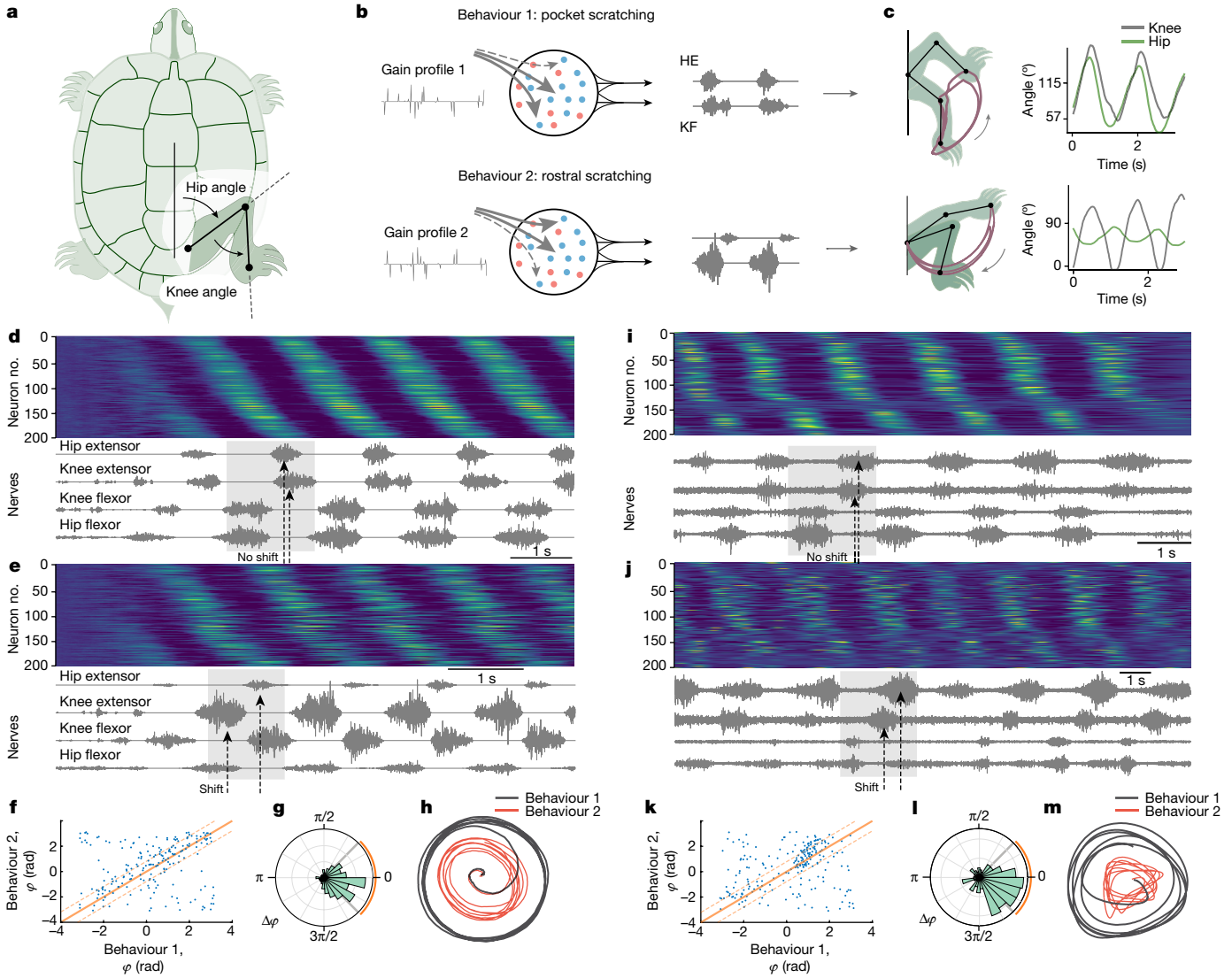

Fig. 5 | Two motor programs in model and experiment. a, Hindlimb movement is quantified using the hip and knee angles. **b**, Two distinct motor behaviours (pocket and rostral scratching) are evoked in the BSG model by distinct gain profiles (left) of neuronal subsets. HE, hip extensor; KF, knee flexor. **c**, The evoked motor patterns (top: pocket; bottom: rostral) translated to limb trajectory (left, brown) and joint angles (right, hip and knee). **d**–**h**, Model results. **d**,**e**, The ensemble activities associated with behaviour 1 (**d**) and behaviour 2 (**e**) are not identical, but resemble one another, although their motor patterns are qualitatively distinct ('no shift' versus 'shift' in the shaded regions). **f**, Phase (φ) of neurons in behaviour 1 versus behaviour 2 with respect to hip flexor scatter around the unity line, shown as ±45°. **g**, Polar histogram of the phase difference ($\Delta\varphi$). The orange line indicates ±45°. **h**, Projection of behaviour 1 (black) and behaviour 2 (red) on the PCs of behaviour 1. Projection of behaviour 2 (red) onto the subspace of behaviour 1 had an overlap of 0.49 compared to its native representation[36] using three PCs. **i**–**m**, Experimental results in a similar arrangement to that in **d**–**h** and similar motor behaviours. Projection of behaviour 2 (red) onto the subspace of behaviour 1 had an overlap of 0.34 compared to its native representation. **a**, Graphic adapted from ref. [35].

trend was seen across trials, behaviours and datasets (Extended Data Fig. 7). Finally, we tested whether other distinct motor patterns could be evoked in the BSG model. A plethora of patterns or 'gaits' could be induced through different gain profiles, with a similar diversity to that of real motor patterns (Extended Data Fig. 8). This suggests that activating a spinal network to generate a desired motor pattern in general translates to finding the appropriate combination of neurons to modulate (for example, by trial-and-error-based motor learning)[37].

Discussion

We have presented evidence that, rather than exhibiting alternating activity, the spinal network behind rhythmic movement exhibits low-dimensional dynamics that can be described as a rotation in neural space. During motor programs, the activity of the spinal population continuously cycles through all phases, whereas the resulting nerve activity is alternating (Fig. 1). Using computational modelling, we have shown that the core function of a spinal CPG (that is, to convert a constant input to a rhythmic motor output) can be achieved by a simple balanced network that undergoes a transition to an oscillatory state. The alternating nerve activity is then obtained by a readout from certain phases of the rotational population activity (Fig. 2). This model stands in contrast to conventional CPG theories that rely on cellular properties for rhythm generation and a modular hierarchy for pattern generation[1,2].

It is important to note that our theory of rotation does not exclude the role of specific cell types[4] (for example, for left–right coordination or speed control[29,30]) and that cell-type-specific connectivity could be included in the model to obtain a theoretical understanding of its effect on the resulting neural dynamics[38]. Similarly, the role of intrinsic cellular

properties (for example, nonlinear adaptation) could be included to elucidate their role in shaping network oscillations[27]. However, as there is rich diversity among spinal interneurons (with, for instance, more than 50 subsets of the GABAergic interneuron[39]), inclusion of only partial cell-type mappings is unlikely to offer better insight into the dynamical properties of the network. Such complexity is not necessary to explain rotational dynamics.

The BSG model has all phases represented evenly in the population, which is a result of the simplified random connectivity (Fig. 2b). Skewed phase representation could be achieved by including more structured connectivity, such as variable degrees of convergence and divergence while keeping the E/I balance. The random connectivity in our model was chosen as the most parsimonious structure in the absence of an experimentally derived core CPG connectome. However, the mechanism we propose to be behind the rotational dynamics could be found in other types of network architecture. Random connectivity is therefore not a requirement for our theory of rotational dynamics.

This theory also explains 'deletions', during which nerve bursts are missing whereas the overall rhythmic pattern continues (Extended Data Fig. 9). Depending on the exact readout direction (which would probably involve PCs beyond the first three), even a relatively modest change in the population trajectory could cause a large change (for example, a deletion) in the readout (Extended Data Fig. 10). This suggests that a separation of spinal rhythm- and pattern-generating layers, as previously proposed[2], is not necessary to account for deletions.

The ability to generate multiple movement patterns has already been studied for cortical networks[25,28,33,34], but the issue of multifunctionality in spinal motor networks has remained an open question. In our model, we explored a mechanism to generate multiple rhythmic motor patterns in the same spinal network by gain modulation of a subset of neurons in the network. Such subset modulation could be accomplished by cellular nodes that distribute sparse input to a larger population, as has been observed for spinal motor synergy encoders[40].

Our theory could also be extended to account for non-rhythmic sequences by using a brief and targeted input drive, hence generating a single cycle of neural rotation, sculpted by selective gain modulation in the spinal network through descending commands from the brain. This could provide an important link between the motor circuits for rhythmic movement and those for non-rhythmic sequences, which is missing at present.

Online content

Any methods, additional references, Nature Research reporting summaries, source data, extended data, supplementary information, acknowledgements, peer review information; details of author contributions and competing interests; and statements of data and code availability are available at https://doi.org/10.1038/s41586-022-05293-w.

1. Grillner, S. & El Manira, A. Current principles of motor control, with special reference to vertebrate locomotion. *Physiol. Rev.* **100**, 271–320 (2020).
2. McCrea, D. A. & Rybak, I. A. Organization of mammalian locomotor rhythm and pattern generation. *Brain Res. Rev.* **57**, 134–146 (2008).
3. Arber, S. & Costa, R. M. Connecting neuronal circuits for movement. *Science* **360**, 1403–1404 (2018).
4. Gosgnach, S. et al. Delineating the diversity of spinal interneurons in locomotor circuits. *J. Neurosci.* **37**, 10835–10841 (2017).
5. Goulding, M. Circuits controlling vertebrate locomotion: moving in a new direction. *Nat. Rev. Neurosci.* **10**, 507–518 (2009).
6. Stein, P. S. G. & Daniels-McQueen, S. Modular organization of turtle spinal interneurons during normal and deletion fictive rostral scratching. *J. Neurosci.* **22**, 6800–6809 (2002).
7. Petersen, P. C. & Berg, R. W. Lognormal firing rate distribution reveals prominent fluctuation-driven regime in spinal motor networks. *eLife* **5**, e18805 (2016).
8. Radosevic, M. et al. Decoupling of timescales reveals sparse convergent CPG network in the adult spinal cord. *Nat. Commun.* **10**, 2937 (2019).
9. Russo, A. A. et al. Motor cortex embeds muscle-like commands in an untangled population response. *Neuron* **97**, 953–966 (2018).
10. Churchland, M. M. et al. Neural population dynamics during reaching. *Nature* **487**, 51–56 (2012).
11. Sussillo, D. et al. A neural network that finds a naturalistic solution for the production of muscle activity. *Nat. Neurosci.* **18**, 1025–1033 (2015).
12. Bruno, A. M. et al. A spiral attractor network drives locomotion in *Aplysia*. *eLife* **6**, e27342 (2017).
13. Berkinblit, M. B. et al. Generation of scratching. I. Activity of spinal interneurons during scratching. *J. Neurophysiol.* **41**, 1040–1057 (1978).
14. Auyong, N. et al. Preferred locomotor phase of activity of lumbar interneurons during air-stepping in subchronic spinal cats. *J. Neurophysiol.* **106**, 1943–1953 (2011).
15. Kwan, A. C. et al. Spatiotemporal dynamics of rhythmic spinal interneurons measured with two-photon calcium imaging and coherence analysis. *J. Neurophysiol.* **104**, 3323–3333 (2010).
16. Kiehn, O. et al. Excitatory components of the mammalian locomotor CPG. *Brain Res. Rev.* **57**, 56–63 (2008).
17. Rancic, V. & Gosgnach, S. Recent insights into the rhythmogenic core of the locomotor CPG. *Int. J. Mol. Sci.* **22**, 1394 (2021).
18. Dayan, P. & Abbott, L. F. *Theoretical Neuroscience: Computational and Mathematical Modeling of Neural Systems* (MIT Press, 2001).
19. Hennequin, G., Agnes, E. J. & Vogels, T. P. Inhibitory plasticity: balance, control, and codependence. *Annu. Rev. Neurosci.* **40**, 557–579 (2017).
20. Berg, R. W., Willumsen, A. & Lindén, H. When networks walk a fine line: balance of excitation and inhibition in spinal motor circuits. *Curr. Opin. Physiol.* **8**, 76–83 (2019).
21. Berg, R. W., Alaburda, A. & Hounsgaard, J. Balanced inhibition and excitation drive spike activity in spinal half-centers. *Science* **315**, 390–393 (2007).
22. Machado, T. A. *Probing Circuits for Spinal Motor Control*. PhD thesis, Columbia Univ. (2015).
23. Ramirez, J.-M. & Baertsch, N. A. The dynamic basis of respiratory rhythm generation: one breath at a time. *Annu. Rev. Neurosci.* **41**, 475–499 (2018).
24. Rajan, K., Abbott, L. F. & Sompolinsky, H. Stimulus-dependent suppression of chaos in recurrent neural networks. *Phys. Rev. E* **82**, 011903 (2010).
25. Hennequin, G., Vogels, T. P. & Gerstner, W. Optimal control of transient dynamics in balanced networks supports generation of complex movements. *Neuron* **82**, 1394–1406 (2014).
26. van Vreeswijk, C. & Sompolinsky, H. Chaos in neuronal networks with balanced excitatory and inhibitory activity. *Science* **274**, 1724–1726 (1996).
27. Beiran, M. & Ostojic, S. Contrasting the effects of adaptation and synaptic filtering on the timescales of dynamics in recurrent networks. *PLoS Comput. Biol.* **15**, e1006893 (2019).
28. Stroud, J. P., Porter, M. A., Hennequin, G. & Vogels, T. P. Motor primitives in space and time via targeted gain modulation in cortical networks. *Nat. Neurosci.* **21**, 1774–1783 (2018).
29. Gosgnach, S. et al. V1 spinal neurons regulate the speed of vertebrate locomotor outputs. *Nature* **440**, 215–219 (2006).
30. Callahan, R. A. et al. Spinal V2b neurons reveal a role for ipsilateral inhibition in speed control. *eLife* **8**, e47837 (2019).
31. Berkowitz, A. et al. Roles for multifunctional and specialized spinal interneurons during motor pattern generation in tadpoles, zebrafish larvae, and turtles. *Front. Behav. Neurosci.* **4**, 36 (2010).
32. Briggman, K. L. & Kristan, W. B. Multifunctional pattern-generating circuits. *Annu. Rev. Neurosci.* **31**, 271–294 (2008).
33. Sussillo, D. & Abbott, L. F. Generating coherent patterns of activity from chaotic neural networks. *Neuron* **63**, 544–557 (2009).
34. Logiaco, L., Abbott, L. & Escola, S. Thalamic control of cortical dynamics in a model of flexible motor sequencing. *Cell Rep.* **35**, 109090 (2021).
35. Mortin, L. I., Keifer, J. & Stein, P. S. Three forms of the scratch reflex in the spinal turtle: movement analyses. *J. Neurophysiol.* **53**, 1501–1516 (1985).
36. Elsayed, G. F., Lara, A. H., Kaufman, M. T., Churchland, M. M. & Cunningham, J. P. Reorganization between preparatory and movement population responses in motor cortex. *Nat. Commun.* **7**, 13239 (2016).
37. Gallego, J. A., Perich, M. G., Miller, L. E. & Solla, S. A. Neural manifolds for the control of movement. *Neuron* **94**, 978–984 (2017).
38. Aljadeff, J., Stern, M. & Sharpee, T. Transition to chaos in random networks with cell-type-specific connectivity. *Phys. Rev. Lett.* **114**, 088101 (2015).
39. Bikoff, J. B. et al. Spinal inhibitory interneuron diversity delineates variant motor microcircuits. *Cell* **165**, 207–219 (2016).
40. Levine, A. J. et al. Identification of a cellular node for motor control pathways. *Nat. Neurosci.* **17**, 586–593 (2014).

Methods

In this Methods section, we describe the experimental protocols and the details of our computational modelling. The experimental data have been used in a previous study for a different purpose[7].

Experimental methods

The surgical procedures comply with Danish legislation and were approved by the controlling body (The Animal Experiments Inspectorate) under the Ministry of Food, Agriculture and Fisheries of Denmark (permission number 2018-15-0201-01504). Methods have previously been published in detail[7,8,41]. In brief, successful experiments on four adult (approximately 5 years of age) red-eared turtles (*Trachemys scripta elegans*), ordered from Nasco (https://www.enasco.com/), of both sexes formed the basis of this study. One of the animals was used twice on different days, resulting in a total of five datasets. The animal was placed on crushed ice for 2 h to ensure hypothermic anaesthesia[41], then killed by decapitation, and its blood was substituted by perfusion with a Ringer solution containing 120 mM NaCl, 5 mM KCl, 15 mM $NaHCO_3$, 2 mM $MgCl_2$, 3 mM $CaCl_2$ and 20 mM glucose, saturated with 98% O_2 and 2% CO_2 to obtain pH 7.6. The carapace containing the D4–S2 spinal cord segments was isolated by transverse cuts, and the cord was perfused with Ringer's solution through the vertebral foramen, by means of a steel tube and silicone gasket pressing against the D4 vertebra. The motor nerves were cut to measure their activity and increase mechanical stability by preventing movements of the limbs. The preparation was placed on the back and fixed with glue in a chamber with a constant flow of oxygenated Ringer's solution to keep the cord submerged and the skin tissue moist[41]. The vertebrae (D8–D10) corresponding to the lumbar segments L2–L5 in mammals[42] were carefully opened on the ventral side to allow access to the spinal cord for insertion of the multi-electrode arrays. We opened the spinal column on the ventral side along segments D8–D10 and gently removed the dura mater with a fine scalpel and forceps. For each insertion site of the multi-electrode arrays, the pia mater was opened with longitudinal cuts along the spinal cord with the tip of a bent syringe needle tip (BD Microlance 3: 27G 3/4 in, 0.4 × 19 mm). The cuts were made in parallel in the ventral horn between the ventral roots. Blinding and randomization of the data collection was not applicable in this study.

Electrophysiology

To monitor the rhythmic activity and motor program state, electroneurogram recordings were performed using suction electrodes on the hip flexor, knee extensor and dD8 nerves[43] (that is, a total of six motor nerves (three from each side) at the level of the D9–D10 vertebrae). The electroneurograms were recorded with a differential amplifier (Iso-DAM8, World Precision Instruments) with the filter bandwidth at 300 Hz to 1 kHz, and sampled at 20 kHz with a 12-bit analog-to-digital converter (Digidata 1200, Axon Instruments), displayed by means of Axoscope and Clampex software (Axon Instruments). Custom-designed silicon probes were inserted into the lumbar spinal cord (D8, D9 and D10) in the anterior–posterior direction to minimize damage to the white matter fibre tracks. These segments correspond to the lumbar (L2–L5) spinal cord in mammals[42]. Up to four 64-channel silicon probes (that is, 256 recording sites) were inserted (Berg64 from NeuroNexus). The probes had eight shanks and eight recording sites on each shank arranged in a staggered configuration with 30 µm vertical distance. The shanks had a thickness of 15 µm and were spaced 200 µm apart. Recordings were performed in parallel at 40 kHz using a 256-channel multiplexed amplifier (KJE-1001, Amplipex) to acquire the extracellular potentials of a large number of neurons, for post hoc polytrode spike sorting.

Motor network activation by cutaneous sensory input

Each scratch episode lasted approximately 20 s. A new trial was initiated after a 5-min rest. To reproducibly activate the scratching motor pattern, a linear actuator was applied to provide mechanical touch on the skin around the legs meeting the carapace. The somatic touch was controlled by a function generator (TT2000, Thurlby Thandar Instruments) and consisted of a 10-s-long sinusoidal movement (1–2 Hz). The touch was applied on the border of the carapace marginal shields M9–M10 and the soft tissue surrounding the hindlimb, which is the receptive field for inducing the pocket scratching motor pattern. Pocket scratching was elicited on either the right or the left side on the soft tissue surrounding the hindlimb representing two distinct behaviours. Further, the rostral scratching behaviour was elicited by similar touching of the carapace in the more rostral location on the shields. For reviews on the various motor patterns and the cutaneous activation, see refs. [31,44].

Five experimental datasets that fulfilled the requirements of both successful recording from large numbers of neurons, six motor nerve recordings, and activation of distinct motor behaviours were acquired. A summary of the parameters is shown in Supplementary Table 1. The electrode depths are indicated with respect to the ventral side, which puts the electrode arrays in Rexed laminae VII–VIII, where the motor-related interneurons are located.

Data analysis

All data analysis was performed in custom-designed procedures in Matlab (Mathworks, R2020b) or Python (https://www.python.org). Spike sorting was performed using KlustaKwik[45]. Spike rates were estimated by convolving the neuronal spike times with a Gaussian kernel

$$k(t) = \frac{1}{\sqrt{2\pi}\sigma}\exp\left(-\frac{t^2}{2\sigma^2}\right)$$

in which σ = 250 ms, to capture the slow modulation of the firing rate. The firing rates were further high-pass filtered with a three-pole Butterworth filter using a zero-phase filter (filtfilt.m) function in Matlab, with a cutoff frequency of 0.3 Hz. To better visualize the phase of neuronal activity, the firing rate amplitude was normalized to unity and the mean was subtracted. The nerve activity was rectified and band-pass filtered from 0.2 to 5 Hz. This data filtering was performed on all of the data except the data involved in linear decoding, for which the slow components are an important element in the translation between population spiking and the nerve output.

Principal component analysis. Principal component analysis (PCA) of the multidimensional population firing rates was performed on the firing rate space (neural space). The principal components U_n were determined as eigenvectors of the empirical covariance matrix C of the n firing rate traces, with the eigenvalues λ_n representing the absolute amount of variance in the data that each component can account for. The eigenvectors and eigenvalues were found through

$$\mathbf{CU} = \mathbf{U\Sigma}$$

in which $\mathbf{U} = [U_1, U_2, \ldots, U_n]$ contains the PCs (eigenvectors) U_n and

$$\mathbf{\Sigma} = \begin{bmatrix} \lambda_1 & 0 & \ldots \\ \vdots & \ddots & \\ 0 & & \lambda_n \end{bmatrix}$$

The PCA was performed in Matlab using the function PCA.m. A similar PC analysis was performed on the nerve activity, although these were only six-dimensional data (Fig. 1). The neuronal population activity plotted in PC space as a function of time was achieved by projecting the population vector, $\mathbf{r}(t) = [r_1(t), \ldots, r_n(t)]$ (that is, a vector with the firing rates of all neurons), onto the PCs, giving the population vector in new coordinates, $\mathbf{r}'(t)$:

$$\mathbf{r}'(t) = \mathbf{r}(t)\mathbf{U}$$

Subspace overlap analysis. A method for quantifying to what extent a PC subspace of one behaviour overlaps that of a different behaviour has been introduced previously[36]. To quantify the overlap between the low-dimensional subspaces of two different behaviours, we first computed the PCs of the two behaviours separately using PCA (see above). We then selected the first three PCs as their respective subspace. The overlap between subspaces was then calculated as the total variance captured by a projection of the first behaviour on the PCs of the other behaviour, divided by the variance captured by the projection onto its 'native' PCs[36]. We used the first three PC dimensions for this quantification in both experiments and model simulations (Fig. 5 and Extended Data Fig. 7).

Sorting of units according to motor phase. The firing rate of units was sorted according to motor phase through two steps. First, the frequency of rhythmic activity was identified by estimating the peak in the power spectrum of a representative nerve. For this purpose, the nerve activity was rectified and smoothed and subsampled to have the same sampling rate as the estimated firing rates. Second, the magnitude and phase of the coherence Coh_i between this nerve activity and the firing rate of the ith neuron was estimated through[46]

$$\mathrm{Coh}_i(f) = \frac{\sum_{j=1}^{k} R_{ij}(f) N_j(f)}{k\sqrt{S_{xxi}^2 S_{\mathrm{nerve}}^2}}$$

in which k is the number of multi-taper spectral estimates ($k = 4$). R_{ij} and N_j are the individual spectral estimates using the discrete Fourier transform of the tapered firing rate of the ith neuron, $r_i(t)$, and the rectified and low-pass-filtered nerve trace $n(t)$:

$$R_{ij}(f) = \sum_{t=0}^{T} \mathrm{e}^{j2\pi ft} r_i(t) w_j(t)$$

$$N_j(f) = \sum_{t=0}^{T} \mathrm{e}^{j2\pi ft} n(t) w_j(t)$$

and $w_j(t)$ is the jth taper function, the discrete prolate spheroidal (Slepian) sequences[47]. These taper functions and the Fourier transforms were calculated using the Matlab functions dpss.m and fft.m. The power spectra of the firing rate of the ith neuron and the nerve were calculated as $S_{xxi}^2 = \frac{1}{k}\sum_{j=1}^{j=k} R_{ij}R_{ij}^*$ and $S_{\mathrm{nerve}}^2 = \frac{1}{k}\sum_{j=1}^{j=k} N_j N_j^*$, in which the asterisks indicate a complex conjugate. The phase of the ith neuron was chosen from $\mathrm{Coh}_i(f)$ at the frequency for which the strongest peak in S_{nerve}^2 was found, which was the rhythm of the motor pattern. On the basis of the phase, the neurons were sorted and their activity was plotted (for example, Fig. 1c).

Nerve activity measures. In some of the analysis, the motor output was measured as electroneurograms quantified using the root mean square (r.m.s.) of the traces after smoothing using the Savitzky–Golay finite impulse response filter. The r.m.s. of the electroneurograms are:

$$\mathrm{ENG}_{\mathrm{r.m.s.}} = \sqrt{\frac{1}{n}(x_1^2 + x_1^2 + \ldots + x_n^2)}$$

in which $x_1, x_2, \ldots, x_n$ are the electroneurogram (ENG) measurements and n is the number of samples. The r.m.s. values were calculated in Matlab using the procedure rms.m. The mean values reported (Fig. 3g) are the average of all six nerves. The error bars are the standard error of the means (that is, the standard deviation divided by $\sqrt{6}$). A pairwise statistical comparison was performed between trials, each having six measurements (the nerves), using the non-parametric Wilcoxon signed rank test through the procedure singrank.m in Matlab.

The relationship between the radius of PC rotation (r.m.s. of the first two components) and nerve output (r.m.s.) was verified using an F-statistic versus a constant model. The test statistic for the F-test on the regression model (Extended Data Fig. 6g,h) is a test of whether the linear fit is significantly better than a constant.

Nerve output prediction using a linear decoder. Linear decoding of neural ensembles (for example, in the primary motor cortex) has been used efficiently to control prosthetic devices using a brain–computer interface for individuals with tetraplegic conditions[48,49]. The idea is to use a linear filter, $\mathbf{f}$ (that is, a linear decoder), that can translate the firing rates of a population of neurons, written as a matrix $\mathbf{R} = \mathbf{r}(t)$ over a time period, to a readout to control a set of muscles, $\mathbf{N}$, such that $\mathbf{N} = \mathbf{Rf}$. The filter is first constructed from training data that describe the association between the firing rate matrix $\mathbf{R}$ and the nerve output matrix $\mathbf{N}$ (Extended Data Fig. 10). The filter was estimated using the least-squares formulation from a closed-form expression[50]:

$$\mathbf{f} = (\mathbf{R}^{\mathbf{T}}\mathbf{R})^{-1}\mathbf{R}^{\mathbf{T}}\mathbf{N}$$

In this study, we form a prediction of the nerve output based on the linear decoding of the neuronal population activity in the spinal cord, for the intention of verifying how well a population measure can predict the output. This is relevant for the investigation of deletions. The prediction of deletions purely from the sampled population activity can give insight into whether there are several layers in the motor network (that is, separation of rhythm and pattern generation), which has previously been proposed to explain non-resetting deletions in decerebrated cats and spinal cords isolated from neonatal rodents[2,51–53].

Trajectory tangling metric of neuronal population and nerve activity. The degree of tangling of the trajectories in neural space compared with that of the motor nerve trajectories has recently been quantified by a new metric[9,54]. We use this metric to quantify trajectory tangling in this study (Extended Data Fig. 3). In brief, the metric is the point in the multidimensional state space $\mathbf{r}(t)$, which can represent either the population firing rate or the activity of the group of motor nerves (six in our case), or the PCs thereof. The tangling, $Q(t)$, is defined as the maximum squared Euclidean difference in velocity of the movement along the trajectory at two points in time, t and t', $\mathbf{r}'(t) - \mathbf{r}'(t')$, divided by the Euclidean distance between the points squared:

$$Q(t) = \max_{t'} \frac{||\dot{\boldsymbol{r}}_{\boldsymbol{t}} - \dot{\boldsymbol{r}}_{\boldsymbol{t'}}||^2}{||\boldsymbol{r}_{\boldsymbol{t}} - \boldsymbol{r}_{\boldsymbol{t'}}||^2 + \boldsymbol{\epsilon}}$$

This fraction is a basic measure of how different the velocity (speed and direction) is between two points on the curve divided by how far they are from each other. The unit of Q is s^{-2}. If the trajectory is very tangled, there will be points that have different directions and are close to each other. Parts of the trajectory with low tangling will tend to move in the same direction if they are close to each other. ε is a small constant added to avoid division by zero. The value of ε is not important if it is small compared with the scale of the data. Similarly, the scale of the data should not affect the tangling metric if it is large compared with ε. As we are comparing firing rates and ENG nerve recording, which differ by several orders of magnitude, we scaled ε by the r.m.s. of the first PC. The derivative was estimated as the difference in $\mathbf{r}$ between neighbouring samples and divided by the sampling time. As this method tends to enhance noise, we first smoothed the trace with a kernel (500 point, Savitzky–Golay of second degree). We calculated the tangling of the first three PCs of firing rates of the neuronal population and compared it with the tangling of the first three components of the six-dimensional nerve activity. We used the fraction of time points for which the tangling was higher for the nerves than for the network as a composite measure to compare across trials and animals (Extended Data Fig. 3).

Statistics and reproducibility

For Fig. 1, data were acquired in ten independent trials for that animal (eight trials shown in Extended Data Fig. 1). Similar measurements were performed over five independent data sessions (four animals) with a total of 28 trials of one behaviour (Extended Data Fig. 2). For Fig. 3, data were acquired in five independent data sessions (four animals) with a total of 49 trials. See also Extended Data Fig. 7. For Fig. 5, data were acquired in five independent data sessions (four animals) with a total of 49 trials. See also Extended Data Fig. 7.

BSG network model

The model consists of a network of interneurons and two or more nerve readouts that represent the motor commands resulting from the network activity.

Interneuron network. The interneuron network consists of $N = 200$ neurons, of which half are excitatory and half are inhibitory. We model the activity of an example neuron i as a firing rate $r[g_i(t), V_i(t)]$ that depends on an activity variable $V_i(t)$, analogous to a membrane potential, and a gain variable $g_i(t)$. We use a similar function to that used in previously published model[28] adjusted to avoid negative firing rates:

$$r(g_i, V_i) = \begin{cases} V_*(1 - \tanh[g(V - V_*)/V_*]), & \text{for } V \le V_* \\ V_* + V_{\max} \tanh[g(V - V_*)/V_{\max}], & \text{for } V > V_* \end{cases}$$

in which V_* represents the input level at which the slope of the firing rate function has its maximum (resulting in an output firing rate of $r = V_*$ (Hz)) and $V_{\max}$ is the maximum deviation (in terms of firing rates) from V_*. Here we set $V_* = 20$ and $V_{\max} = 50$, resulting in a maximum firing rate of 70 Hz. The dynamics of the network is determined by

$$\tau \dot{V}_i(t) = -V_i(t) + \sum_j W_{ij} r[g_j(t), V_j(t)] + I_e(t)$$

in which $\tau = 50$ ms is a time constant representing the combined membrane and synaptic timescale, W is a matrix that describes the network connectivity (see below), and $I_e(t)$ is a time-varying external drive that consists of a constant input and a noise term $I_e(t) = I(t) + \nu$, in which the noise term ν is Gaussian noise with zero mean and a standard deviation of 4. The network thus receives two types of external input: a common external input ('drive') I_e that is used to cause a transition from a quiet state to an active rhythmic state (Fig. 2), and an input that sets the gain g_i of individual neurons that is used to modulate the network activity in terms of amplitude (Fig. 3), frequency (Fig. 4) or for multifunctional behaviour (Fig. 5). For simplicity we used a constant input drive $I_e = 20$ when studying the effects of gain modulation in the network.

Network connectivity. The connectivity of the network is assumed to be sparse[8] with a pairwise connection probability $C = 0.1$. The synaptic weights in the network are assumed to be balanced; that is, excitatory (positive) weights, w_{ex}, are equal in magnitude to inhibitory (negative) ones, w_{in}. To ensure that the incoming connections are balanced for each neuron, we construct the connectivity matrix W as follows. We start with a matrix in which all elements are zero. For each neuron, we then select $CN/2$ presynaptic excitatory neurons and assign them the weight w_{ex} and $CN/2$ presynaptic inhibitory neurons and assign them the weight w_{in}. In this way, we ensure that the network is both globally and locally balanced[55] (that is, the incoming synaptic weights are balanced for each neuron). The synaptic weights are set according to

$$w_{ex} = \frac{1}{\sqrt{NC(1-C)}}$$

with $w_{in} = -w_{ex}$ (ref. [56]). This results in a connectivity matrix W with a spectral radius of 1 (Fig. 2d); that is, the largest eigenvalue $\lambda_{max} = 1$ on average over network realizations. The dynamical stability of the network dynamics is determined by the external input I_e, the network connectivity W and the gain parameter g and can be analysed using linear stability analysis of the effective connectivity matrix gW (see the mathematical note in the Supplementary Information). A unity spectral radius of the connectivity matrix combined with a uniform gain $g = 1$ results in a network that is on the edge of instability. As a default, we set $g = 1.2$ resulting in a linearly unstable network. Furthermore, as not all randomly connected networks are expected to generate oscillations (see the mathematical note in the Supplementary Information), here we selected only connectivity matrices for which the largest eigenvalue λ_{max} had a nonzero imaginary part.

Gain modulation for amplitude control. To control the amplitude of oscillations in the network model, we adjusted the gain parameter g uniformly for all neurons in the network. As a larger neuronal gain results in a larger firing rate for the same synaptic input, the overall amplitude of the oscillatory activity can be expected to increase as the neuronal gain is increased in the network.

Gain modulation for frequency control: speed and brake cells. To control the frequency of oscillations in the network, we adjusted the gain g_i individually for selected neurons in the network. A simple procedure was set up to estimate the influence of each neuron on the overall frequency. The gain g_i was increased and decreased by a small amount, and the spectrum of the effective connectivity matrix gW was calculated (Fig. 4a). Depending on whether that imaginary part of the largest eigenvalue λ_{max} was increased or decreased (corresponding to an expected increased or decreased oscillation frequency), we assigned the neuron a rank depending on its frequency modulation capacity. A positive modulation capacity means that an increase in gain or drive to that neuron will increase the frequency of the rhythm, and vice versa for a negative modulation index. As a detailed gain modulation of all neurons in the network can be considered less biologically plausible, we selected the 10% of neurons with the largest positive effect on the imaginary part and labelled them as speed cells, and the 10% with the largest negative effect and labelled them brake cells. To increase the network oscillation frequency, we increased the gain of the speed cells and decreased the gain of the brake cells (Fig. 4). To decrease the network oscillation frequency, we did the opposite (that is, we decreased the gain of the speed cells and increased the gain of the brake cells).

Gain modulation for multifunctional activity: switch cells. To generate different motor behaviour from the network, we identified a subset of neurons that had a large influence on the neuronal phase distribution of the dominant eigenmode. Starting with a default value for the gain of $g = 1.1$, we first calculated the phase for each interneuron from the eigenvector corresponding to the largest eigenvalue of the effective connectivity matrix gW. We then increased the gain g_i of each neuron i individually and calculated the effect on the phase distribution of the now slightly different effective connectivity. The top 10% of the neurons that caused the largest change in the overall phase distribution, calculated as the circular standard deviation of the change in phase, were selected as switch neurons. To generate two different distinct behaviours, we set the gain of the switch neurons to two different random vectors with values uniformly distributed in the range $g_i = 1.1 \pm 0.3$. The circular standard deviation was calculated using circular statistics as originally defined in ref. [57] (section 2.3.3):

$$\sigma_{\text{circular}} = \sqrt{-2 \log[\bar{R}]}$$

(where log is the natural logarithm of $\bar{R}$ which is the mean resultant length of all observations in polar coordinates; hence, $\bar{R}$ is between

0 and 1). If the observed angles are close to each other, the resultant length is close to 1 and σ_{circular} is close to 0.

Nerve readout. The nerve activity was modelled using a Gaussian noise with zero mean and for which the standard deviation $\sigma(t)$ of the distribution depends on a threshold-linear readout from the interneuron network:

$$\sigma(t) = \left[\sum_i M_i \phi_i(t)\right]_+ \quad (1)$$

in which M_i represents the readout weights and $[]_+$ indicates that the width can only be positive. The readout weights were constrained to respect Dale's law; that is, excitatory interneurons could only have positive weights and inhibitory interneurons could only have negative weights. We used two different ways of setting up the linear readout.

For readout based on the phase of the dominant eigenmode, the simplest method used was to use readout weights M_i based on the phase of each neuron i in the network oscillation. The phase of all neurons was estimated from the eigenvector corresponding to the largest eigenvalue $\lambda_{\max}$ of the connectivity matrix W. To set up the readout for a specific nerve, we first assigned the nerve a phase θ_{nerve}. For excitatory neurons that had a phase of $\theta_{\text{nerve}} \pm \pi/8$ we set $M_i = 1$, and set $M_i = 0$ for all other excitatory neurons. To generate reciprocal inhibition in the nerve input, we selected inhibitory neurons with a phase of $(\theta_{\text{nerve}} + \pi) \pm \pi/8$and set $M_i = -1$, and $M_i = 0$ for all others. To set up a pair of flexor–extensor nerves with alternating activity, we set $\theta_{\text{flexor}} = \pi/2$ and $\theta_{\text{extensor}} = -\pi/2$.

For optimized readout for multifunctional output, we first selected two distinct gain vectors for pocket and rostral scratching behaviour, respectively (see above), and simulated network activity using these gain vectors. To find the appropriate readout weights, we then set up sinusoidal target functions for the nerve function 'input' (that is, the sum in equation (1)) for each behaviour and for each nerve separately. The flexor and extensor nerves were phase-shifted by π. The pocket and rostral scratching behaviours had different relative timing between the knee and hip flexor nerves, shifted by π as well as different amplitudes (Fig. 5). Readout weights were then found using a linear least-squares algorithm with bounds on the variables (implemented in Python using scipy.optimize.lsq_linear) such that the weights M_i could only be positive for excitatory neurons and negative for inhibitory neurons.

To translate the nerve readout to the position of the knee and foot, we set up a simple model that integrates the nerve drive to calculate the angle Θ of the foot–knee joint resulting from the flexor and extensor nerves (Fig. 5 and Supplementary Video 3):

$$\tau_{\text{muscle}} \dot{\Theta}(t) = w_\Theta[\text{flexor}(t) - \text{extensor}(t) - (\Theta - \Theta_0)]$$

in which $\tau_{\text{muscle}} = 10$ ms represents the timescale with which a muscle responds to a motor drive and w_Θ is a weight that gives the force resulting from a specific drive. The last term on the right-hand side represents a weak decay back to the initial joint position of the limb. Joint angles were limited to be within $[0,\pi]$.

Reporting summary

Further information on research design is available in the Nature Research Reporting Summary linked to this article.

Data availability

Data are available through a link to an online repository, which can be found on the laboratory web page (https://berg-lab.net/) or on reasonable request from the corresponding authors.

Code availability

The Python code that was used for simulating the BSG network is available in an online repository (https://github.com/BergLab/BSG). The Matlab code for analysing the experimental data is available on the laboratory web page (https://berg-lab.net/) or on reasonable request from the corresponding authors.

41. Berg, R. W. in *The Neural Control of Movement* (eds Whelan, P. J. & Sharples, S. A.) 205–219 (Elsevier, 2020).
42. Walloe, S. et al. Stereological estimate of the total number of neurons in spinal segment D9 of the red-eared turtle. *J. Neurosci.* **31**, 2431–2435 (2011).
43. Bannatyne, B. A. et al. Neurotransmitters and motoneuron contacts of multifunctional and behaviorally specialized turtle spinal cord interneurons. *J. Neurosci.* **40**, 2680–2694 (2020).
44. Stein, P. S. G. Central pattern generators in the turtle spinal cord: selection among the forms of motor behaviors. *J. Neurophysiol.* **119**, 422–440 (2018).
45. Kadir, S. N. et al. High-dimensional cluster analysis with the masked EM algorithm. *Neural Comput.* **26**, 2379–2394 (2014).
46. Berg, R. W. et al. Exploratory whisking by rat is not phase locked to the hippocampal theta rhythm. *J. Neurosci.* **26**, 6518–6522 (2006).
47. Percival, D. B. & Walden, A. T. *Spectral Analysis for Physical Applications - Multitaper and Conventional Univariate Techniques* (Cambridge Univ. Press, 1998)
48. Bonizzato, M. et al. Multi-pronged neuromodulation intervention engages the residual motor circuitry to facilitate walking in a rat model of spinal cord injury. *Nat. Commun.* **12**, 1925 (2021).
49. Hochberg, L. R. et al. Neuronal ensemble control of prosthetic devices by a human with tetraplegia. *Nature* **442**, 164–171 (2006).
50. Serruya, M. D. et al. Instant neural control of a movement signal. *Nature* **416**, 141–142 (2002).
51. Dougherty, K. J. & Ha, N. T. The rhythm section: an update on spinal interneurons setting the beat for mammalian locomotion. *Curr. Opin. Physiol.* **8**, 84–93 (2019).
52. Lafreniere-Roula, M. & McCrea, D. A. Deletions of rhythmic motoneuron activity during fictive locomotion and scratch provide clues to the organization of the mammalian central pattern generator. *J. Neurophysiol.* **94**, 1120–1132 (2005).
53. Zhong, G. et al. Neuronal activity in the isolated mouse spinal cord during spontaneous deletions in fictive locomotion: insights into locomotor central pattern generator organization. *J. Physiol.* **590**, 4735–4759 (2012).
54. Suresh, A. K. et al. Neural population dynamics in motor cortex are different for reach and grasp. *eLife* **9**, e58848 (2020).
55. Vogels, T. P. & Abbott, L. F. Gating multiple signals through detailed balance of excitation and inhibition in spiking networks. *Nat. Neurosci.* **12**, 483–491 (2009).
56. Kanaka, R. & Abbott, L. F. Eigenvalue spectra of random matrices for neural networks. *Phys. Rev. Lett.* **97**, 188104 (2006).
57. Mardia, K. V. & Jupp, P. E. *Directional Statistics* (Wiley, 2000).

Acknowledgements This work was supported by The Independent Research Fund Denmark and Mobilex (number 8020-00436B, DFF–1333-00226A), the Carlsberg Foundation (number CF18-0845) and the Lundbeck Foundation (number R366-2021-233).

Author contributions R.W.B. conceived the original experiments. P.C.P. set up and performed the experiments, collected the data and analysed some of the data. M.V., H.L. and R.W.B. conceived the original theory. H.L. performed the model simulations. H.L. and R.W.B. designed and developed the theory, analysed the experimental data and wrote the manuscript.

Competing interests The authors declare no competing interests.

Additional information

Supplementary information The online version contains supplementary material available at https://doi.org/10.1038/s41586-022-05293-w.

Correspondence and requests for materials should be addressed to Henrik Lindén or Rune W. Berg.

Peer review information *Nature* thanks the anonymous reviewers for their contribution to the peer review of this work. Peer reviewer reports are available.

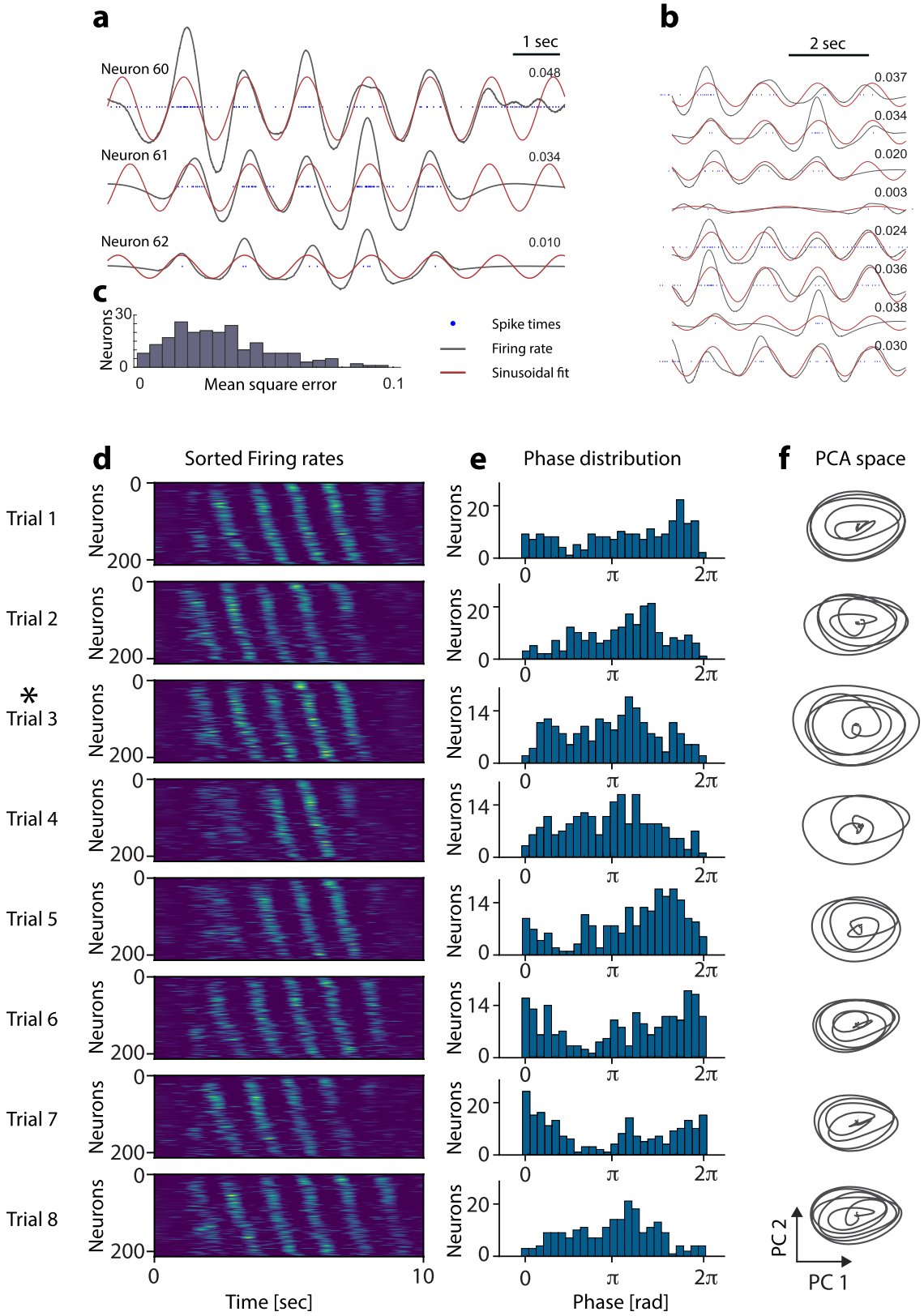

Extended Data Fig. 1 | See next page for caption.

Extended Data Fig. 1 | Firing rate is rhythmic with rotational population dynamics across trials in the lumbar spinal motor network during rhythmic movement. a, The firing rates of 3 sample units (black) with their spike times indicated as blue dots. A sinus function was fitted to the firing rate (red) and the mean square error is indicated (bottom right). b, More sample units, with the mean square error indicated to the left. c, Distribution of mean square errors for the population (n = 214). The mean square error is unitless, since the firing rates were high pass filtered and normalized (maximal firing is 1). d, The firing rates (normalized, color coded) of 214 spinal neurons in laminae VII-VIII as a function of time and sorted according to phase with respect to the nerve activity (hip flexor). Eight consecutive trials from same experiment with a 5 min pause in between each. e, The phase distribution across the neuronal population. f, The population activity has rotational dynamics, as demonstrated by the circular motion of the first two PCs. The PCs were calculated by the data of one trial (trial 3, "*") and the applied to the rest of the trials. The sorting of neurons was according to their phase relation with representative nerve for one trial (also trial 3, "*") and this order was maintained for the rest of the trials. Bottom scale bars represent 1000.

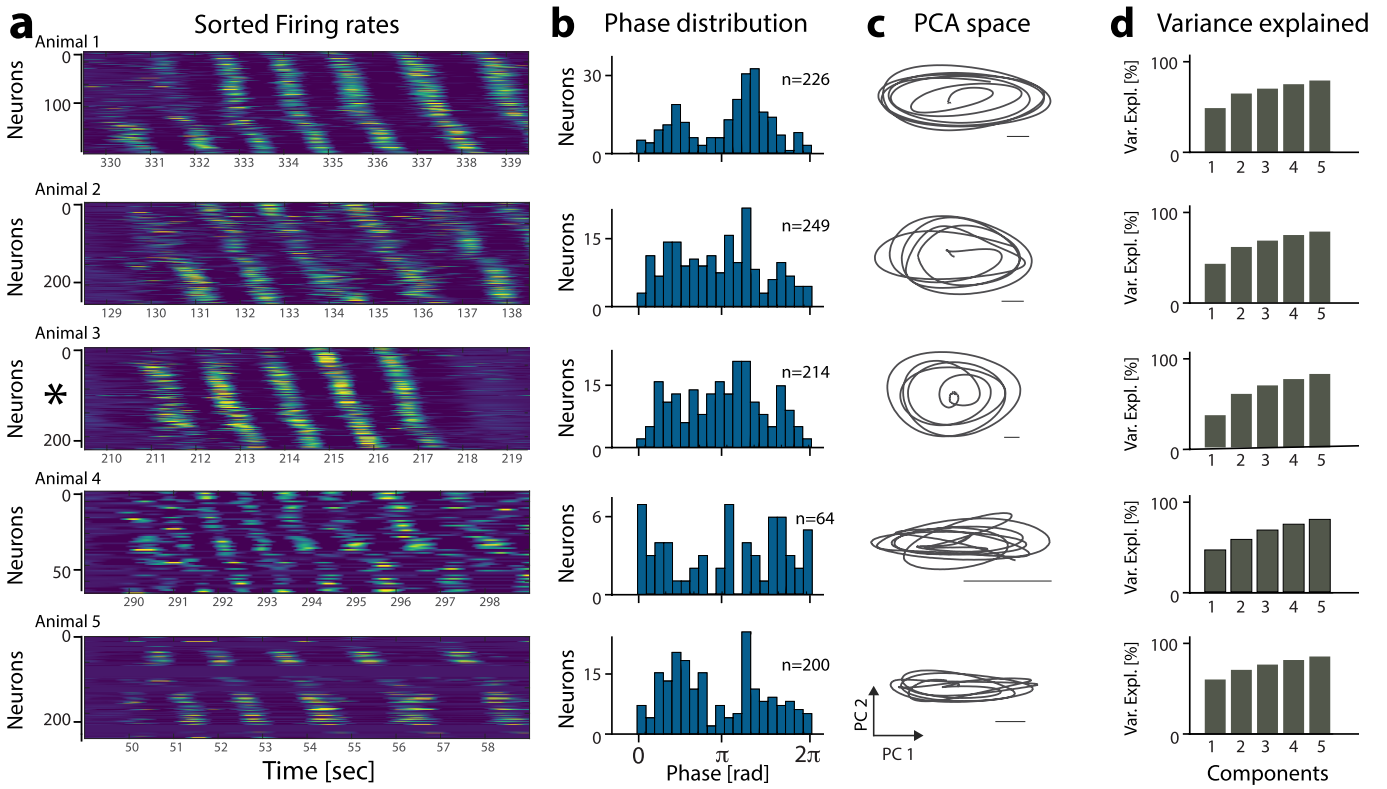

Extended Data Fig. 2 | Rotational population dynamics in a spinal motor network across animals. a, The rhythmic firing rates in populations of spinal neurons in laminae VII-VIII shown in colors as a function of time and sorted according to phase with respect to a nerve (hip flexor). A representative trial from 5 experiments of approximately 10 s demonstrate similar sequential/rotational population activity. Animal used in Extended Data Fig. 1 is marked "*". b, The corresponding distribution of neurons having preferred phases among the population of rhythmic neurons. c, Population activity represented by first two PCs exhibit rotational dynamics. Scale bars: 250. d, Cumulative explained variance by principal components, indicating the population dynamics is low-dimensional, i.e. most of the variance is captured by few components.

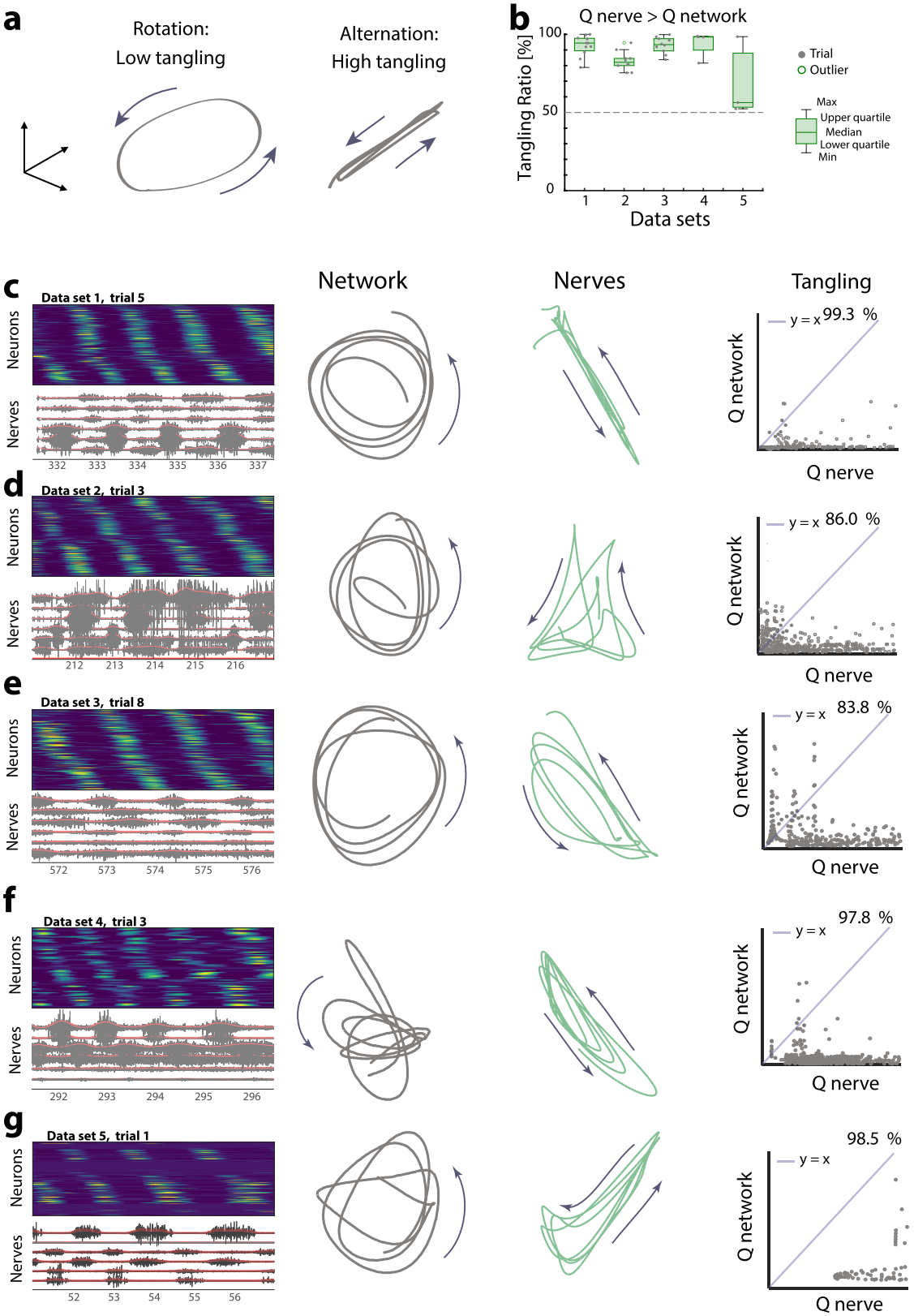

Extended Data Fig. 3 | See next page for caption.

Extended Data Fig. 3 | Neuronal population trajectories in PC-space have lower tangling than the corresponding motor nerve trajectories. a, Illustration that during rotational dynamics the points in the trajectory that move in opposite direction are also far apart, i.e. they have low tangling (left), whereas during alternation the points of the trajectory that move in opposite direction are also close, i.e. have high tangling (right). b, The ratio of tangling metric of the PC trajectory of the nerves (Q_{nerve}) to that of the network ($Q_{network}$). This ratio is close to 100%, which indicates most trials and animals had a larger tangling of the motor nerves than the network. (N = 11, data set 1; N = 10, data set 2; N = 10, data set 3; N = 4, data set 4; N = 3, data set 5). c–g, Sample trials from 5 different data sets. Left is shown the phase sorted firing rate activity (top) and the associated nerves (bottom). The nerves were rectified and low-pass filtered (red) on temporal scale matching the firing rates. The PCs of network (middle left) and nerves (middle right, green). Scales of PCs are variance normalized. The tangling metric (Q) for the nerve PCs (in 3 dimensions) is calculated as a function of time (t) through the trial and plotted versus that for the network. The ratio of points below the $x = y$–line (pale blue) is indicated in percent and form one point in panel (b). Note that the nerve trajectories more resemble "alternation" whereas the network more resembles "rotation"-scheme of (a).

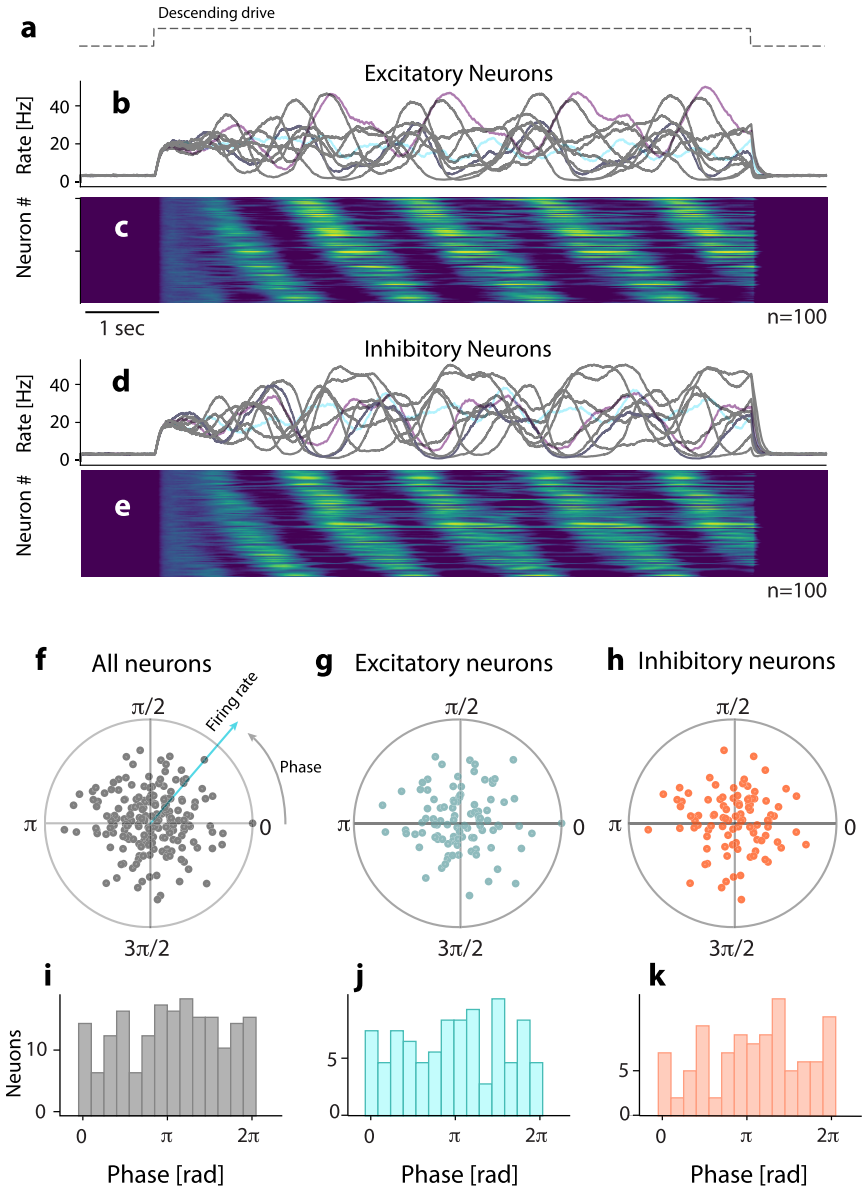

Extended Data Fig. 4 | Rotational ensemble activity within the excitatory and inhibitory sub-populations in the BSG-model. a, Activation of the motor circuit by descending drive. b, The firing rates of 10 sample excitatory neurons oscillate because of the descending input. (c) Sorting the excitatory neurons according to phase of firing rates reveals a sequential activity like the previously observed for all neurons. d-e, Activity and similar sorting of the inhibitory sub-populations reveals similar sequential and rotational dynamics within that sub-population. f, The network eigenmode for the whole network: Each dot represent both the phase (the polar angle) and the peak firing rate (the radius) for a given neuron (n = 200). g-h, Similar plot for the excitatory and inhibitory populations. i-k, the distribution of phases in linear histograms for all neurons (i), excitatory (j) and inhibitory neurons (k). To be compared with experimental distributions (Extended Data Figs. 1 and 2).

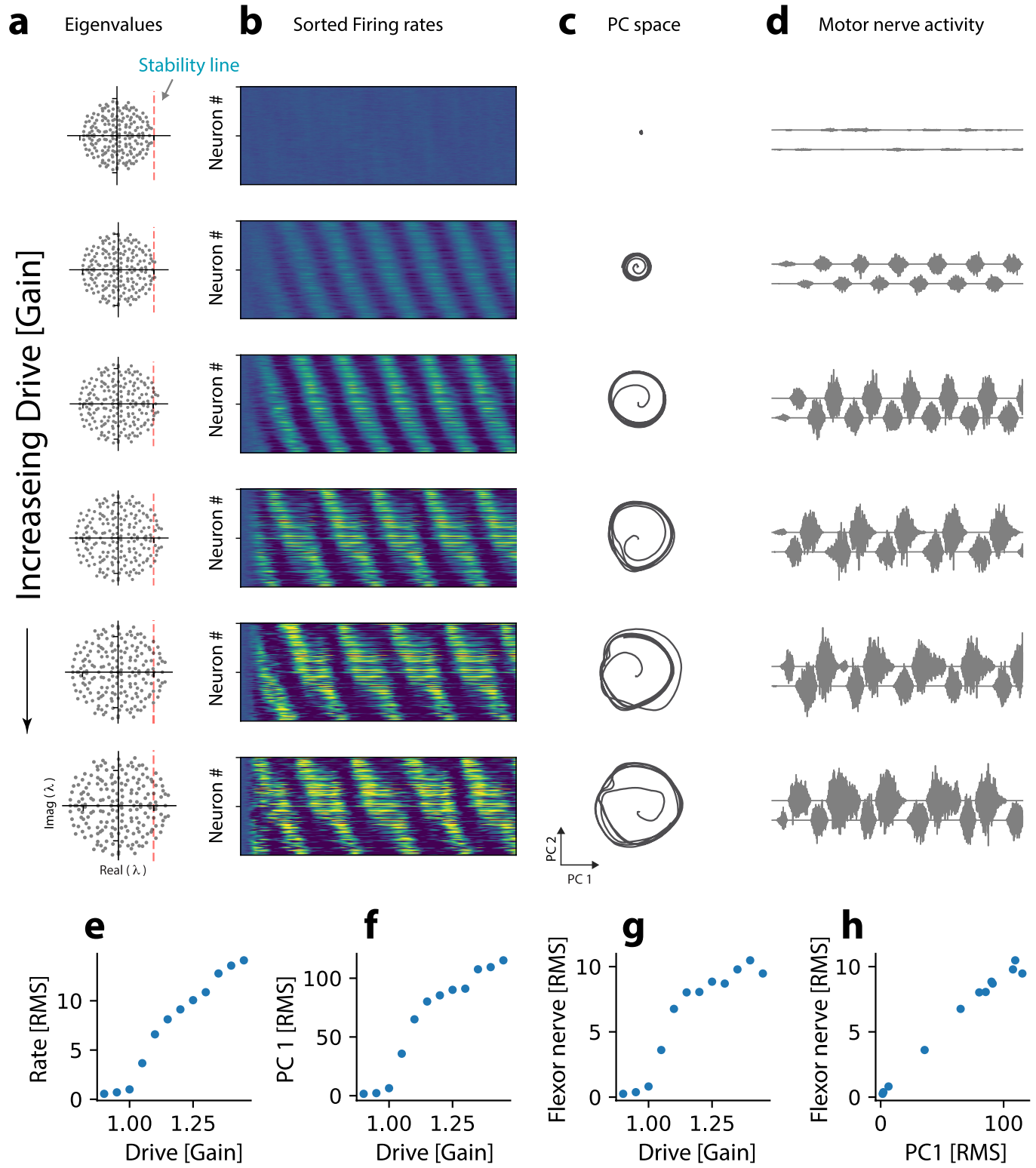

Extended Data Fig. 5 | BSG-model: Correlation between descending drive and radius of rotation as well as amplitude of nerve output without affecting the period. a, For low neuronal gain (top), the eigenvalue spectrum does not have any eigenvalues that cross the stability line (broken vertical line). As the gain increases (downward direction) the spectrum expands, and eigenvalues cross the stability line. For larger gain the eigenvalues cross the stability line farther. b, The associated population dynamics (sorted firing rates) exhibit oscillation of increasing magnitude as the drive increase. c, The rotational dynamics also has a radius that increases with increasing drive. d, The resulting motor nerve output is also increasing in amplitude. e, Descending drive (gain) versus the population firing rate (RMS), radius of rotation in PC space, f, and amplitude of nerve output (flexor RMS), g. h, the radius of rotation (PC1RMS) vs. the nerve amplitude (flexor RMS).

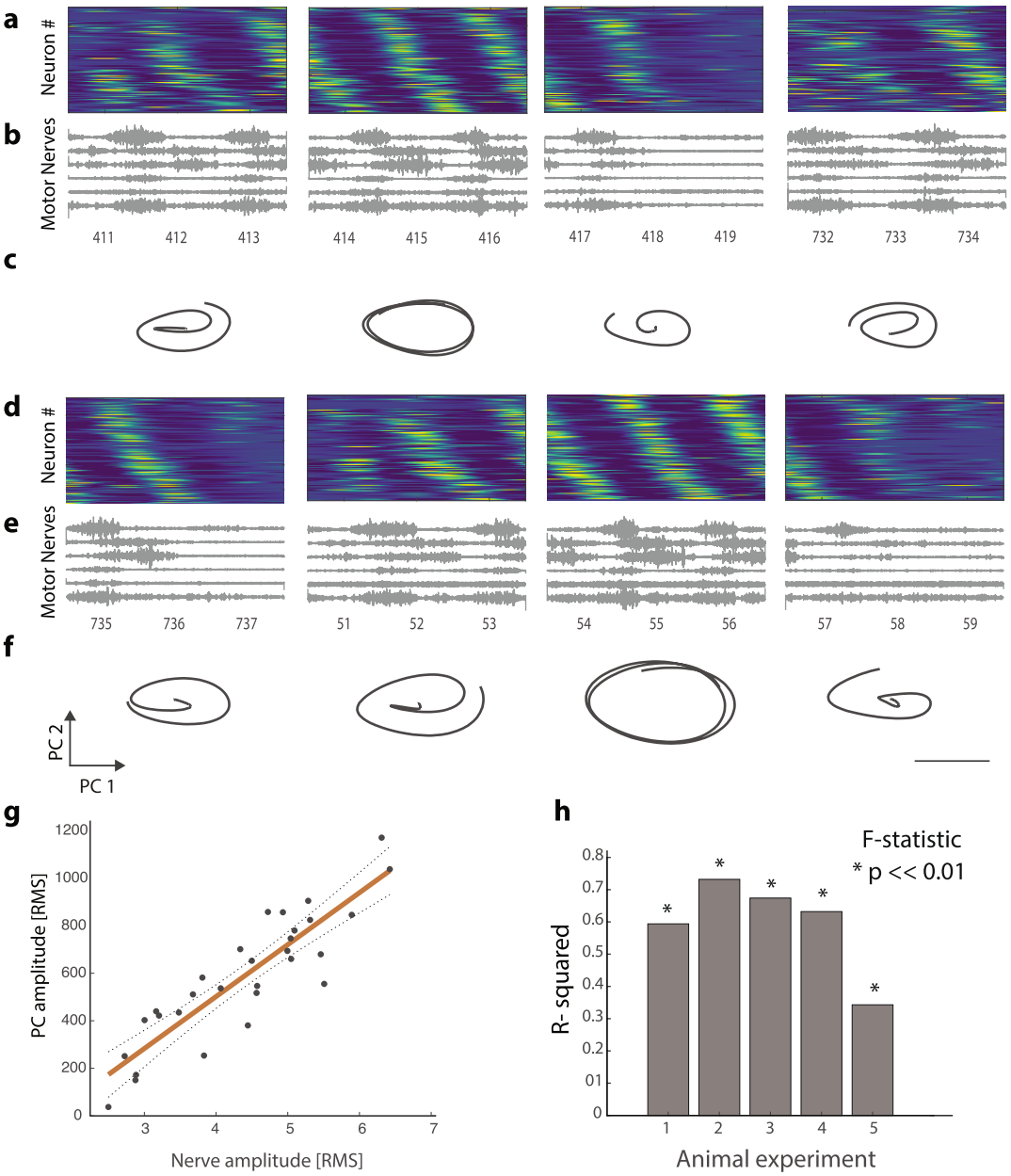

Extended Data Fig. 6 | Radius of rotation correlates with nerve output in experiment. a, Sample trial where the population activity was divided up in pieces with the corresponding nerve output b. c, The PC manifolds had rotation with varying radius. d-f, other pieces with same organization. g, The RMS of the nerve activity versus the RMS of the first two PCs for various pieces of activity had a significant correlation (F-statistic of rejection of no trend at p«0.01). h, The R^2 values for all animal tested (n=5). *: F-statistic of rejection of null hypothesis of zero correlation at p«0.01. f, Scale bar: 1000.

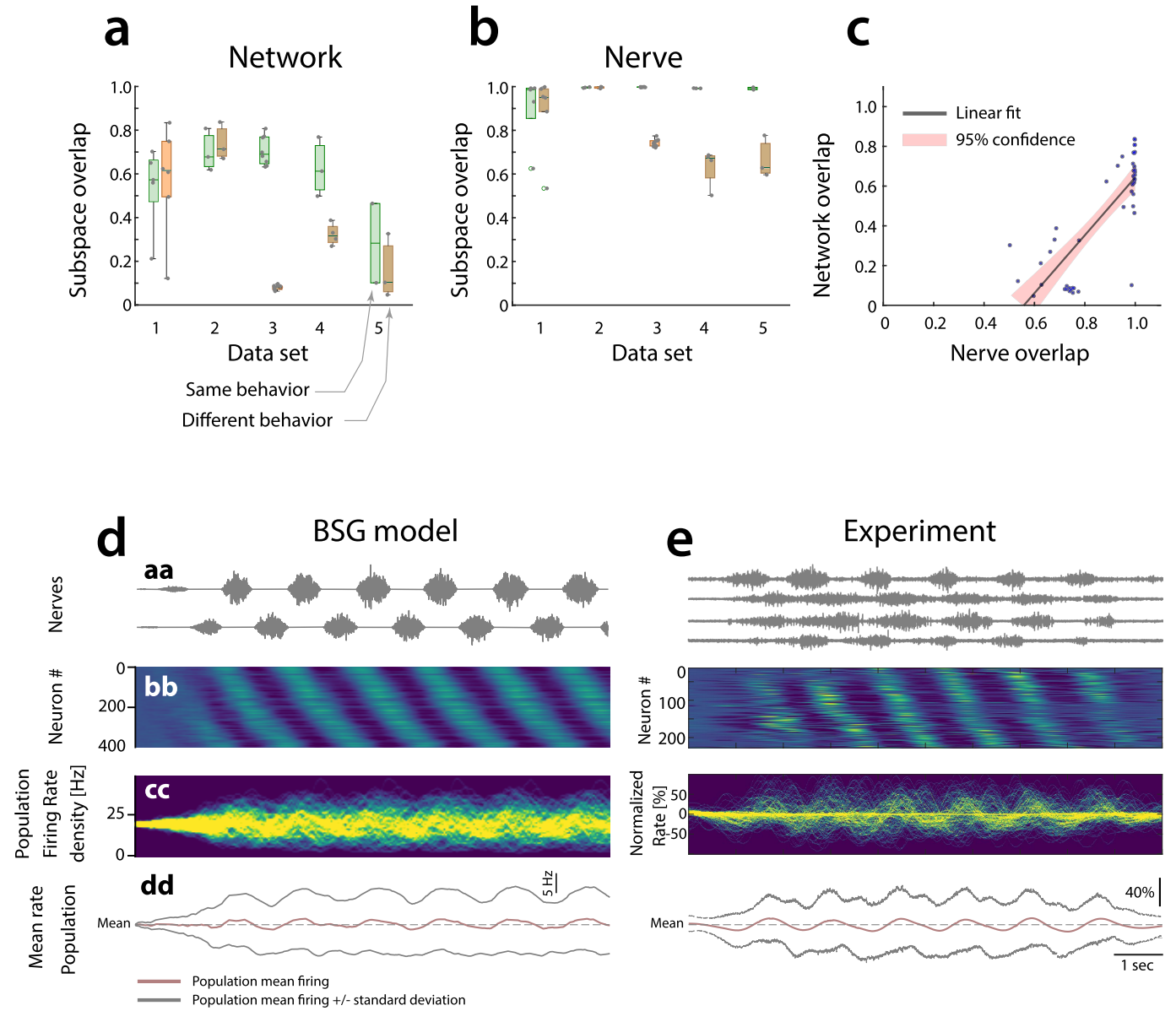

Extended Data Fig. 7 | Representation of one behavior in the subspace of another behavior. a, The variance captured by the projection of the network dynamics onto the first three PCs of another trial (green) normalized by the variance captured by the PCs of its own dynamics. Orange: the subspace-overlap of a different behavior. Independent samples: N= Same behavior/ different behavior, N = 5/6, data set 1; N = 3/3, data set 2; N=8/10, data set 3; N = 3/4, data set 4; N = 2/3, data set 5). Whisker plots represent min and max values. Box plots represent median −25% and +75% quartiles. b, the subspace representation of the nerve activity of same behavior (green) and a different behavior (orange). N=Same behavior / different behavior: N = 5/6, data set 1; N = 3/3, data set 2; N = 8/10, data set 3; N = 3/4, data set 4; N = 2/3, data set 5). Whisker plots represent min and max values. Box plots represent median −25% and +75% quartiles. c, Nerve overlap plotted against the network overlap. A large overlap in nerve output is associated with a large overlap in network overlap. Gray line represents a linear fit, red region represents 95% confidence. d-aa, The flexor/extensor nerve output from the BSG-network. e, The sorted neuronal population firing rate (n = 400 neurons) with rotational dynamics. (cc) Color map of the population firing rate. dd, Mean (red) and variance of the population activity. e, same organization as in (d), but for experimental data. Animal no. 3 trial 8.

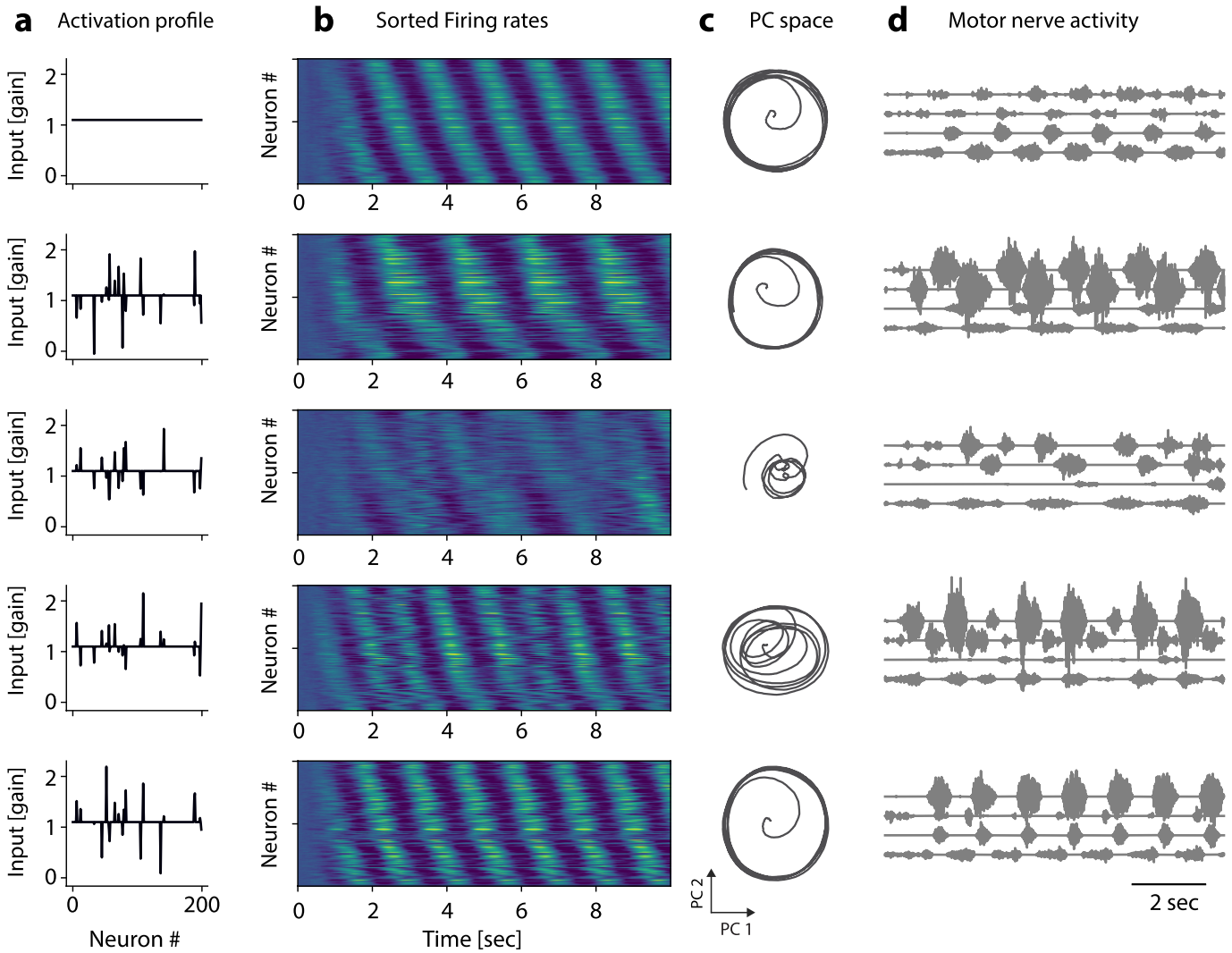

Extended Data Fig. 8 | Multifunctionalism in the BSG-model. a, Five examples of specific activation/modulation of selected neurons in the network ("activation profiles"). The top profile has an even distribution, whereas all the below profiles have selective modulation of specific neurons. b, The ensemble activity as a result of the activation profile show a sequential activity, with similar but not identical sequence of activity. c, The first two PCs, based on the top activation profile, all exhibit rotational dynamics, albeit with different radius and trajectories. (d) the output motor patterns associated with the different activation profiles and ensemble activities.

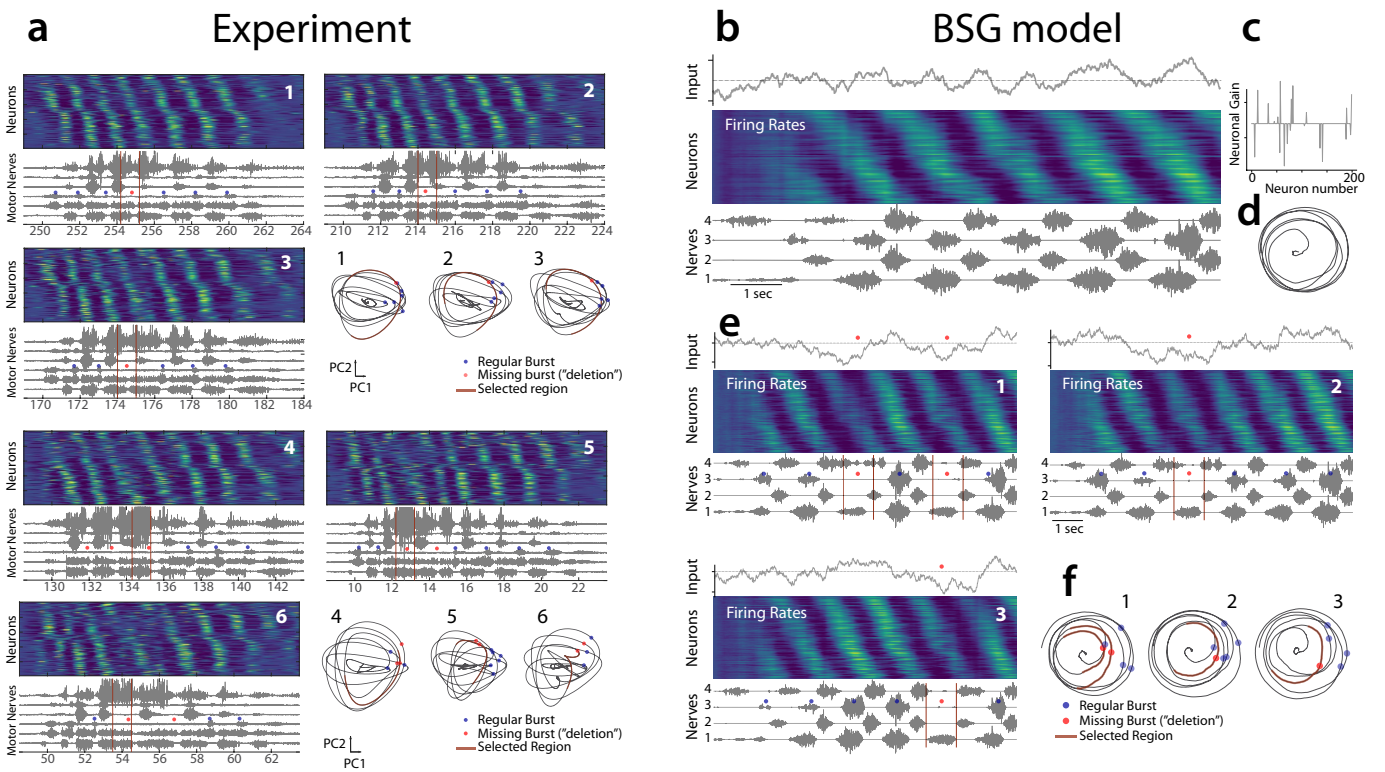

Extended Data Fig. 9 | "Deletions" both in the experimental data and in the BSG model. a, Six trials (1–6) shown with the neuronal firing rates sorted according to phase (color map, top) and the 6 nerves (bottom) during a motor behavior (pocket scratching). The absence of a burst, i.e. a deletion, was observed in the hip extensor nerve recording (red dots) whereas the hip flexor (bottom trace) seems to continue and combine two cycles although with a small decrease. Regular bursts are also indicated (blue dots). The corresponding trajectories in PC-space are shown with the corresponding dots matching the time in the nerve activity. A selected period around the occurrence of one delete is indicated in the nerve traces (red vertical lines). The corresponding time in the trajectory is also indicated in red. Note that deletions tend to occur at smaller radius of the rotation and the population firing rates (color map) are dimmer at those instances. b, A proper motor behavior devoid of "deletions" can be produced by the balanced sequence generator despite receiving a varying input (top). The firing rates for the sorted neuronal population (middle), and the resulting motor nerve output pattern (bottom). c, The appropriate motor program shown in (b) is achieved by a selective gain-modulation, i.e. gain-profile (y-axis), across the neuronal population (x-axis). d, Population activity from (b) represented by in PC-space by the first two components. e, When the varying input transiently becomes too low at a certain phase the nerve cycle is absent, i.e. a "deletion" has occurred (red dots). The firing rates of the neuronal population will be lower at these instances and hence appear dimmer in the color map (middle). A consequent absence of a burst in the nerve is seen (nerve 3, compare red and blue dots). f, the PC-trajectories corresponding to (e) indicated as 1,2 and 3. The temporary distortion of the trajectory at a particular phase is associated with a deletion (red dots). Red parts of the trajectory represent the period between vertical red bars indicated in the nerve activities (d–f). Compare with (a).

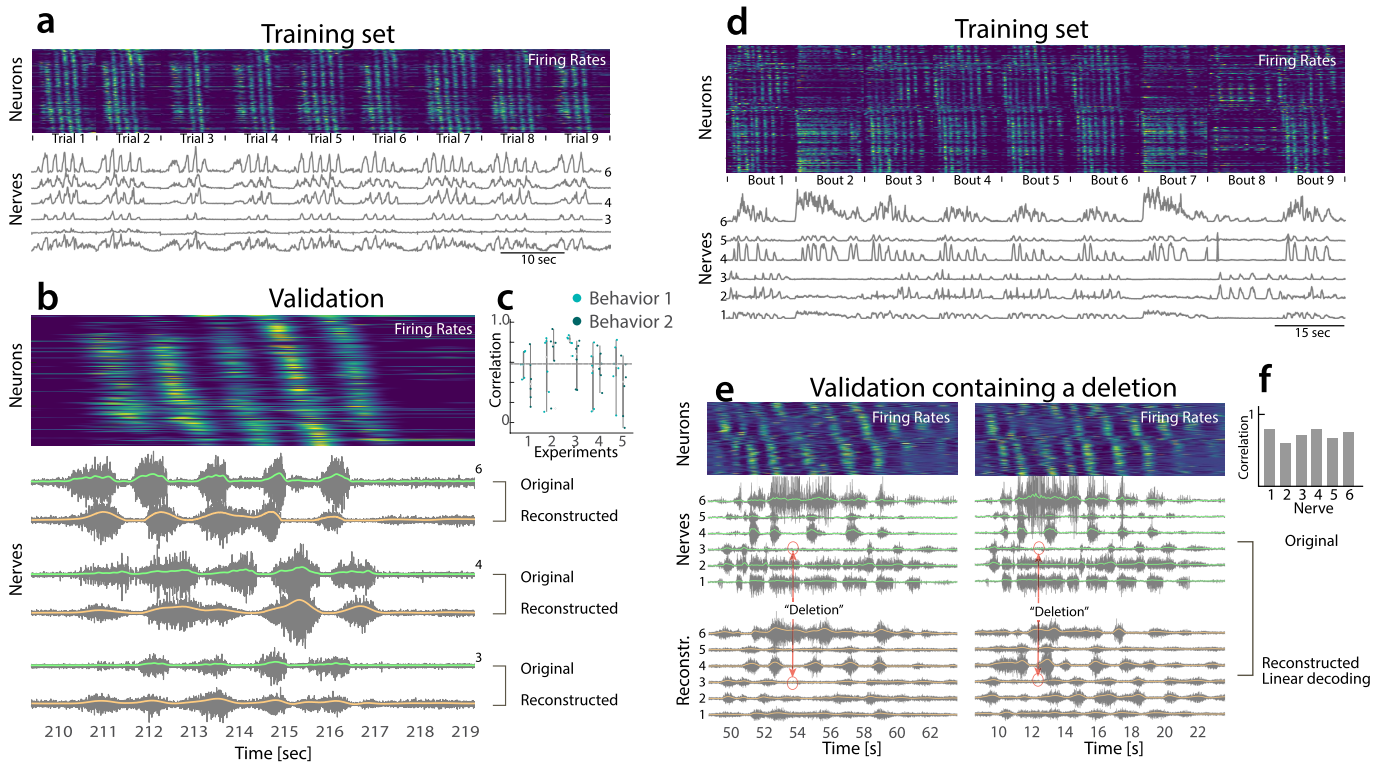

Extended Data Fig. 10 | Reconstruction of nerve output based on linear decoding of neuronal population activity. a, A linear decoder function was estimated using a training set consisting of 9 trials of same behavior. Top: color coded firing rates for the neuronal population (sorted according to phase) with 9 trials concatenated. Bottom: the rectified and low-pass filtered motor nerve output of 6 nerves. b, A trial, that was not included in the training set, is used for validation of the linear decoder. Top: the firing rates of the population, like (a). Bottom: The nerve output of 3 selected nerves (rectified and LP-filtered in green, nerves 3, 4 and 6). The reconstructed standard deviations of the nerves (orange) are multiplied by white Gaussian noise to imitate nerve output (gray). c, the correlation between predicted and actual nerve output for the six nerves (individual dots) are shown for two different motor behaviors (right and left pocket scratching) across the 5 experiments. The median value across all nerves and experiments is $R = 0.6$. All 5 data sets had correlations, which were found significantly different than zero using a t-test of Pearson linear correlation, $p << 0.01$, N = 6. d, Training set consisting of 9 bouts, ie. trials of different motor behaviors, which is used to train a linear decoder function. Top: color coded firing rates for the neuronal population (sorted according to phase) with 9 concatenated bouts. Bottom: the rectified and low-pass filtered motor nerve output of 6 nerves. e, two trials, that was not included in the training set, contained instances of "deletions". Top: the firing rates of the population, like (a). Bottom: The nerve output of 3 selected nerves (rectified and LP-filtered in green, nerves 3, 4 and 6). The reconstructed standard deviations of the nerves (orange) are multiplied by white Gaussian noise to imitate nerve output (gray). f, the correlation between predicted and actual nerve output for the six nerves (individual dots) are shown for two different motor behaviors (right and left pocket scratching) across the 5 experiments. The median value across all nerves and experiments is $R = 0.6$. All 6 correlations were found significantly different than zero using a t-test of Pearson linear correlation, $p << 0.01$, N = 1300 temporal-measurements.

nature portfolio

Corresponding author(s): Rune W. Berg, Henrik Lindén

Last updated by author(s): Jul 7, 2022

Reporting Summary

Nature Portfolio wishes to improve the reproducibility of the work that we publish. This form provides structure for consistency and transparency in reporting. For further information on Nature Portfolio policies, see our Editorial Policies and the Editorial Policy Checklist.

Statistics

For all statistical analyses, confirm that the following items are present in the figure legend, table legend, main text, or Methods section.

n/a	Confirmed	
☐	☒	The exact sample size (*n*) for each experimental group/condition, given as a discrete number and unit of measurement
☐	☒	A statement on whether measurements were taken from distinct samples or whether the same sample was measured repeatedly
☐	☒	The statistical test(s) used AND whether they are one- or two-sided *Only common tests should be described solely by name; describe more complex techniques in the Methods section.*
☒	☐	A description of all covariates tested
☐	☒	A description of any assumptions or corrections, such as tests of normality and adjustment for multiple comparisons
☐	☒	A full description of the statistical parameters including central tendency (e.g. means) or other basic estimates (e.g. regression coefficient) AND variation (e.g. standard deviation) or associated estimates of uncertainty (e.g. confidence intervals)
☐	☒	For null hypothesis testing, the test statistic (e.g. *F*, *t*, *r*) with confidence intervals, effect sizes, degrees of freedom and *P* value noted *Give P values as exact values whenever suitable.*
☒	☐	For Bayesian analysis, information on the choice of priors and Markov chain Monte Carlo settings
☒	☐	For hierarchical and complex designs, identification of the appropriate level for tests and full reporting of outcomes
☒	☐	Estimates of effect sizes (e.g. Cohen's *d*, Pearson's *r*), indicating how they were calculated

Our web collection on statistics for biologists contains articles on many of the points above.

Software and code

Policy information about availability of computer code

Data collection	Amplipex, Clampex
Data analysis	Matlab, Python, KlustaKwik

For manuscripts utilizing custom algorithms or software that are central to the research but not yet described in published literature, software must be made available to editors and reviewers. We strongly encourage code deposition in a community repository (e.g. GitHub). See the Nature Portfolio guidelines for submitting code & software for further information.

Data

Policy information about availability of data

All manuscripts must include a data availability statement. This statement should provide the following information, where applicable:

- Accession codes, unique identifiers, or web links for publicly available datasets
- A description of any restrictions on data availability
- For clinical datasets or third party data, please ensure that the statement adheres to our policy

The datasets generated during and/or analysed during the current study are available from the corresponding author on reasonable request. The code for the model is available on a public repository (reference provided in the manuscript).

Field-specific reporting

Please select the one below that is the best fit for your research. If you are not sure, read the appropriate sections before making your selection.

☒ Life sciences ☐ Behavioural & social sciences ☐ Ecological, evolutionary & environmental sciences

For a reference copy of the document with all sections, see nature.com/documents/nr-reporting-summary-flat.pdf

Life sciences study design

All studies must disclose on these points even when the disclosure is negative.

Sample size	There was no sample size calculation in this study. We base our analysis on 5 collected data sets from 4 animals. Since all 5 data sets was in agreement and lead to the same conclusion, we did not consider it necessary (or ethical) to include more animals.
Data exclusions	No trials or data sets were excluded.
Replication	We have reproduced the finding of rotation in new experiments performed for a different purpose. We have also reproduced the finding of rotation in a rodent (rat) experiment (n=1).
Randomization	There was no randomization in this study. The trials were grouped into what sensory stimulation was performed and which animal it was performed in.
Blinding	Since we were not performing a test of the effect of some agent, blinding was not relevant in this study.

Reporting for specific materials, systems and methods

We require information from authors about some types of materials, experimental systems and methods used in many studies. Here, indicate whether each material, system or method listed is relevant to your study. If you are not sure if a list item applies to your research, read the appropriate section before selecting a response.

Materials & experimental systems

n/a	Involved in the study
☒	☐ Antibodies
☒	☐ Eukaryotic cell lines
☒	☐ Palaeontology and archaeology
☐	☒ Animals and other organisms
☒	☐ Human research participants
☒	☐ Clinical data
☒	☐ Dual use research of concern

Methods

n/a	Involved in the study
☒	☐ ChIP-seq
☒	☐ Flow cytometry
☒	☐ MRI-based neuroimaging

Animals and other organisms

Policy information about studies involving animals; ARRIVE guidelines recommended for reporting animal research

Laboratory animals	Red-eared turtles (Trachemys scripta elegans) of both sexes of age 3-5 years.
Wild animals	This did not involve wild animals.
Field-collected samples	This study did not involve collected samples.
Ethics oversight	The surgical procedures comply with Danish legislation and were approved by the controlling body (The Animal Experiments Inspectorate) under the Ministry of Food, Agriculture and Fisheries of Denmark (permission number 2018-15-0201-01504).

Note that full information on the approval of the study protocol must also be provided in the manuscript.